Journal of Scientific Computing (2025) 104:51
https://doi.org/10.1007/s10915-025-02964-4

A Sparse Hierarchical *hp*-Finite Element Method on Disks and Annuli

Ioannis P. A. Papadopoulos[1] · **Sheehan Olver**[2]

Received: 18 July 2024 / Revised: 6 May 2025 / Accepted: 5 June 2025
© The Author(s) 2025

Abstract
We develop a sparse hierarchical hp-finite element method (hp-FEM) for the Helmholtz equation with variable coefficients posed on a two-dimensional disk or annulus. The mesh is an inner disk cell (omitted if on an annulus domain) and concentric annuli cells. The discretization preserves the Fourier mode decoupling of rotationally invariant operators, such as the Laplacian, which manifests as block diagonal mass and stiffness matrices. Moreover, the matrices have a sparsity pattern independent of the order of the discretization and admit an optimal complexity factorization. The sparse hp-FEM can handle radial discontinuities in the right-hand side and in rotationally invariant Helmholtz coefficients. Rotationally anisotropic coefficients that are approximated by low-degree polynomials in Cartesian coordinates also result in sparse linear systems. We consider examples such as a high-frequency Helmholtz equation with radial discontinuities and rotationally anisotropic coefficients, singular source terms, the time-dependent Schrödinger equation, and an extension to a three-dimensional cylinder domain, with a quasi-optimal solve, via the Alternating Direction Implicit (ADI) algorithm.

Keywords hp-finite element method · Quasi-optimal complexity · Disk · Annulus · Cylinder · Schrödinger equation · High-frequency Helmholtz equation

1 Introduction

In this work, we develop a sparse hierarchical hp-finite element method (hp-FEM) on disks and annuli. The cells in the mesh are stacked concentric annuli where, if the domain is a disk, the innermost cell is a disk. The FEM basis consists of Zernike and Zernike annular polynomials, multivariate orthogonal polynomials in Cartesian coordinates, that are defined on disks and annuli, respectively. The stiffness (weak Laplacian) and mass matrices are sparse and banded irrespective of the polynomial order truncation and the number of cells in the mesh

✉ Ioannis P. A. Papadopoulos
papadopoulos@wias-berlin.de

Sheehan Olver
s.olver@imperial.ac.uk

1 Weierstrass Institute for Applied Analysis and Stochastics, Berlin, Germany

2 Department of Mathematics, Imperial College London, London, UK

Published online: 23 June 2025

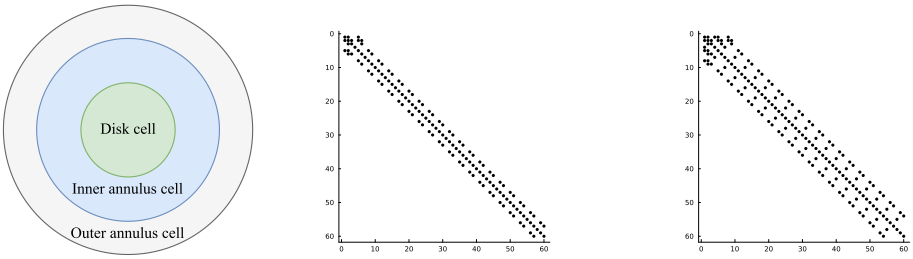

Fig. 1 Meshing a disk domain into 3 cells, an inner disk, and two concentric annuli (left). Spy plots of the first block diagonal submatrix (corresponding to the first Fourier mode) in the stiffness (middle) and mass (right) matrices when truncating the hierarchical basis at degree $N_p = 20$ on each cell in the displayed mesh. The matrices are sparse and banded with a bandwidth independent of N_p

considered. Moreover, for rotationally invariant operators, such as the (weak) Laplacian, the induced matrices are block diagonal where the submatrices correspond to the Fourier mode decoupling. Thus the solve reduces to parallelizable sparse one-dimensional solves for each Fourier mode. In particular, each submatrix along the block diagonal in the Helmholtz operator may be factorized in optimal $\mathcal{O}(N_h N_p)$ complexity. Here N_h denotes the number of cells in the mesh and N_p is the highest degree[1] of the polynomial basis. Thus simply we achieve an $\mathcal{O}(N_h N_p^2)$ optimal complexity solve in two dimensions. After an initial "arrowhead" of size $N_h \times N_h$, the local stiffness and mass submatrices on the block diagonal contain three and five nonzero diagonals, respectively, for increasing degree N_p with minimal coupling across elements. The global stiffness and mass matrices are also block diagonal and the submatrices have a so-called Banded-Block-Banded (B^3) Arrowhead matrix structure with block-bandwidths (1, 1) and (2, 2), respectively, and a sub-block-bandwidth of 1 [32, Def. 4.1]. The mesh and spy plots of the global mass and stiffness submatrices are given in Fig. 1. By considering the tensor-product space of the basis on the disk with a univariate sparse continuous hp-FEM basis for the interval [32], one obtains an FEM basis for the cylinder that is highly effective at handling discontinuities in the radial and z-directions as exemplified in Fig. 2. By leveraging the Alternating Direction Implicit (ADI) algorithm [26], we show one obtains a quasi-optimal $\mathcal{O}(N_h N_p^3 \log(N_h N_p))$ complexity solve for the screened Poisson equation.

Studies on high-order FEM and spectral element methods (SEM) is an extremely active area of research [6, 8, 17, 18, 25]. High-order methods typically lead to fast convergence to the true solution, stabilize discretizations, and avoid pitfalls associated with low-order methods, e.g. locking in linear elasticity [2]. The computational bottleneck is almost always the loss of sparsity, assembly costs, and the ill-conditioning of the matrices that arise after discretization of the equation operators. For many classical FEMs, attempting to assemble the induced mass matrix on a single three-dimensional element with a truncation degree of $N_p = 30$ will surpass the working memory of a standard desktop. One remedy is the use of matrix-free Krylov methods that only require the action of the discretized operators on vectors. However, since the mass and stiffness matrices are often ill-conditioned, a good preconditioner is required in order for the Krylov methods to converge in a reasonable number of iterations [17].

An alternative to using a classical basis, and developing a preconditioner for each problem, is to develop a basis that promotes sparsity in the discretized problem even for a high poly-

[1] FEM and spectral method literature denote the degree by p and n, respectively. We use both conventions in this work, utilizing the notation that is most natural in the context considered.

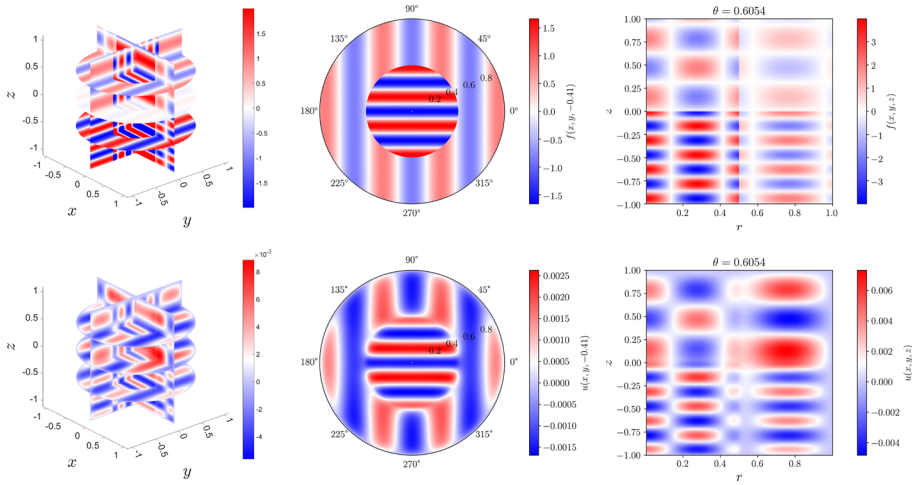

Fig. 2 Plots of the right-hand side, $f(x, y, z)$ (top row) and the solution $u(x, y, z)$ (bottom row) in the screened 3D Poisson equation of Section 6.6 with the right-hand side and Helmholtz coefficient as given in (6.13). The first column is a visualization on the 3D domain and the second and third columns are 2D slices through the (x, y) and z-planes, respectively. Note the discontinuities in $f(x, y, z)$ at $r = 1/2$ and $z = 0$

nomial order and number of elements. The advantage is that the matrices may be explicitly assembled and a direct solver employed for fast convergence. *Sparse* spectral methods may be traced back to the integral reformulation method of Clenshaw, which uses recurrence relationships for integration of Chebyshev polynomials [20]. In 2013, the ultraspherical spectral method was introduced for general ODEs [45] and recently the ultraspherical spectral element method was also developed [25]. Using the ideas of the ultraspherical method as a base, sparse spectral methods were constructed for two-dimensional domains e.g. triangles [46], disks/balls [3, 14, 15, 23, 34, 37, 60, 61], annuli [36, 38], disk slices and trapeziums [56], and spherical caps [57]. The cited works mostly focus on discretizing the strong formulation of the partial differential equation (PDE) which has the disadvantage of not preserving the symmetry of the operators (such as the identity). However, we note that some remedies exist [4].

Utilizing orthogonal polynomials to construct high-order sparse finite element methods stems back to the analysis of the one-dimensional hierarchical p-FEM basis first attributed to Szabó and Babuška [7], see also [58, Ch. 2.5.2] and [52, Ch. 3.1]. The mass and stiffness matrices induced by this basis have a special sparsity structure recently coined as a B^3-Arrowhead matrix structure [32, Def. 4.1]. In [32, Cor. 4.3], it was shown that B^3-Arrowhead matrices permit an optimal complexity $\mathcal{O}(N_h N_p)$ reverse Cholesky factorization, ultimately leading to a quasi-optimal $\mathcal{O}(N_h N_p \log^2 N_p)$ complexity solve for the 1D Poisson equation: from the expansion of the right-hand side to the evaluation of the solution on a grid. Note that other efficient solvers exist, e.g. via static condensation [52, Ch. 3.2].

Extensions to two-dimensional quadrilateral finite elements may be achieved via a tensor-product space of the 1D hierarchical p-FEM basis or by constructing a serendipity element, cf. [5] and [52, Ch. 4.4]. Recently it was shown that the tensor-product space admits, via the ADI algorithm [26], a quasi-optimal $\mathcal{O}(N_h N_p^2 \log^2 N_p)$ solve for the Poisson equation on a quadrilateral domain [32]. Extensions to two-dimensional simplex finite elements have also been considered, e.g. by Babuška et al. [5] as well as Beuchler and Schöberl [13]. Other works

of a similar theme include [10–12, 21, 30, 31] and [56, App. A]. The FEM basis constructed in this work may be thought of as an extension of these other hierarchical bases to the disk.

The choice of the mesh in this work caters towards solving high-frequency Helmholtz equations with radial discontinuities in the Helmholtz coefficient λ and the right-hand side f. We consider such an example in Section 6.2. Unlike spectral method discretizations of the strong form, this approach preserves symmetry and positive-definiteness. This makes it suitable for a unitary preserving discretization of the time-dependent Schrödinger equation via an exponential integrator as considered in Section 6.3. We show that the method can tackle rotationally anisotropic coefficients in Section 6.4 and singular source terms via hp-refinement in Section 6.5. By considering the tensor-product with a univariate basis, the hierarchical basis extends to three-dimensional cylinders. By utilizing the ADI algorithm [26], the three-dimensional solve has $\mathcal{O}(N_h N_p^3 \log(N_h^{1/4} N_p))$ quasi-optimal complexity as discussed in Section 5.

2 Mathematical Setup

Let $\Omega \subset \mathbb{R}^d$, $d \in \{2, 3\}$, denote an open, bounded, and connected domain with a Lipschitz boundary. In this work Ω is a disk, an annulus, or a cylinder. For $0 < a < b$, we denote a disk and annulus domain, respectively, as

$$\Omega_{0,a} := \{(x, y) \in \mathbb{R}^2 : \|(x, y)\|_2 < a\}, \tag{2.1}$$

$$\Omega_{a,b} := \{(x, y) \in \mathbb{R}^2 : a < \|(x, y)\|_2 < b\}, \tag{2.2}$$

where $\|\cdot\|_2$ denotes the Euclidean norm. We use Ω_0 to denote the unit disk $\Omega_0 := \Omega_{0,1}$ and $\Omega_\rho := \Omega_{\rho,1}$, $0 < \rho < 1$, for an annulus with outer radius one.

Let $W^{s,p}(\Omega)$ denote the family of Sobolev spaces [1] and $H^s(\Omega) := W^{s,2}(\Omega)$, $s > 0$. We denote the Lebesgue space by $L^p(\Omega)$, $p \in [1, \infty]$. $H_0^1(\Omega)$ denotes the space of functions that live in $H^1(\Omega)$ that have a boundary trace of zero [27]. Moreover, let $H^{-1}(\Omega)$ denote the dual space of $H_0^1(\Omega)$. If X is a Banach space and H is a Hilbert space, then $\langle \cdot, \cdot \rangle_{X^*,X}$ denotes the duality pairing between a function in X and a functional in the dual space X^* and $\langle \cdot, \cdot \rangle_H$ denotes the inner product in H.

Although we consider more complex equations in Section 6, the canonical equation that exemplifies the core principles of the hp-FEM is the Helmholtz equation with a variable coefficient. The Helmholtz equation seeks a $u \in H_0^1(\Omega)$ that satisfies, for a given $\lambda \in L^2(\Omega)$ and $f \in H^{-1}(\Omega)$:

$$\langle \nabla u, \nabla v \rangle_{L^2(\Omega)} + \langle \lambda u, v \rangle_{L^2(\Omega)} = \langle f, v \rangle_{H^{-1}(\Omega), H_0^1(\Omega)} \quad \text{for all} \quad v \in H_0^1(\Omega). \tag{2.3}$$

If $\lambda \geq 0$ a.e. in Ω, then the existence and uniqueness of u follows as a direct consequence of the Lax–Milgram theorem [24]. In such a regime, the equation is coercive and we hereby refer to this case as the *screened Poisson equation*. In contrast large negative choices of $\lambda < 0$ induce oscillations in the solution which are traditionally hard to resolve with low-order numerical methods.

We now rewrite (2.3) in quasimatrix notation [44]. Let $\Phi = \{\phi_i\}_{i=0}^{\infty}$ denote the set of continuous piecewise polynomials that form the hierarchical basis for $H_0^1(\Omega)$. Then the quasimatrix $\mathbf{\Phi}$ is defined to be a row vector where each entry is a basis function, i.e.

$$\mathbf{\Phi}(x, y) := (\phi_0(x, y) \;\; \phi_1(x, y) \;\; \phi_2(x, y) \;\; \dots). \tag{2.4}$$

Linear operations such as $\frac{\mathrm{d}}{\mathrm{d}x}$ acting on quasimatrices are understood entry-wise. For any function $u \in H^1(\Omega)$, there exists a column coefficient vector $\mathbf{u}$ such that $u(x, y) = \sum_{i=0}^{\infty} \mathbf{u}_i \phi_i(x, y) = \mathbf{\Phi}(x, y)\mathbf{u}$. Throughout this work we expand the right-hand side in a basis of discontinuous piecewise polynomials denoted by Ψ. We define the L^2-inner product between the two quasimatrices $\mathbf{\Phi}$ and $\mathbf{\Psi}$ as follows:

$$\langle \mathbf{\Phi}^\top, \mathbf{\Psi} \rangle_{L^2(\Omega)} := \begin{pmatrix} \langle \phi_0, \psi_0 \rangle_{L^2(\Omega)} & \langle \phi_0, \psi_1 \rangle_{L^2(\Omega)} & \cdots \\ \langle \phi_1, \psi_0 \rangle_{L^2(\Omega)} & \langle \phi_1, \psi_1 \rangle_{L^2(\Omega)} & \cdots \\ \vdots & \vdots & \ddots \end{pmatrix}. \tag{2.5}$$

Rewrite $u(x, y) = \mathbf{\Phi}(x, y)\mathbf{u}$ and consider $f \in L^2(\Omega)$ such that $f(x, y) = \mathbf{\Psi}(x, y)\mathbf{f}$. We define the load vector as $\mathbf{b} := G_{\Phi,\Psi}\mathbf{f}$ where $G_{\Phi,\Psi} := \langle \mathbf{\Phi}^\top, \mathbf{\Psi} \rangle_{L^2(\Omega)}$ is the Gram matrix between Φ and Ψ. We find that the Helmholtz equation (2.3) may be rewritten as find $\mathbf{u}$ that satisfies

$$(A + M_\lambda)\mathbf{u} = \mathbf{b} \tag{2.6}$$

where the stiffness matrix, $A = \langle (\nabla \mathbf{\Phi})^\top, \nabla \mathbf{\Phi} \rangle_{L^2(\Omega)}$, and the weighted mass matrix, $M_\lambda = \langle \mathbf{\Phi}^\top, \lambda \mathbf{\Phi} \rangle_{L^2(\Omega)}$, are symmetric infinite-dimensional matrices. M_λ (provided $\lambda \geq 0$ a.e.) and A are symmetric positive-definite. If $\lambda \equiv 1$ then we drop the subscript $_\lambda$ and call M the mass matrix. The goal of this work is to choose the hierarchical basis Φ with spectral approximation properties that promotes sparsity in the stiffness and mass matrices for an annulus and disk domain.

Remark 2.1 (*Alternative discretizations for disk domains*) Other sparsity preserving discretizations, that decompose the domain, already exist for the disk. A direct extension of the spectral Galerkin method in [53] considers a tensor-product basis of the classical one-dimensional hierarchical p-FEM basis in the radial direction [5, 32] with a Fourier discretization in the angular direction, i.e. the basis functions are of the form $P_n(r)\sin(m\theta + j\pi/2)$, $r \in [0, 1]$, $\theta \in [0, 2\pi)$, $m \in \mathbb{N}$, $j \in \{0, 1\}$, where P_n is a piecewise polynomial of degree n. However, the FEM established in this work has the following advantages:

1. Zernike polynomials often represent functions to the same accuracy with half the degrees of freedom when compared to a Chebyshev $\otimes$ Fourier expansion [15, Sec. 6.2].
2. The discretization preserves symmetry of the PDE operator on annular cells unlike in the spectral Galerkin method found in [53, Sec. 5.2]. Kwan [33] recovered symmetry but the basis functions are nonstandard.
3. $A + M_\lambda$ is approximately twice as sparse as that of a p-FEM $\otimes$ Fourier expansion, with 7 or less nonzero entries per row when λ is piecewise constant.
4. Thanks to the symmetric B^3-Arrowhead structure, the $n \times n$ linear systems admit a simple optimal complexity $\mathcal{O}(n)$ factorization via a reverse Cholesky factorization.
5. On disk domains, there have been several studies showing that discretizations of the form $P_n(r)\sin(m\theta + j\pi/2)$, $r \in [0, 1]$, $\theta \in [0, 2\pi)$, that treat the origin as a boundary point are suboptimal. They suffer from both coordinate singularities and artificially clustered grids at the origin cf. [15, Sec. 6], [61, Sec. 2], [60, Sec. 1]. In turn this leads to worse approximations and numerical instabilities. There are some alternatives, e.g. using double-wrapped Chebyshev [61], leveraging a quadratic argument [15, 33] or, as discussed in this work, one-sided Jacobi polynomials (i.e. Zernike polynomials) that resolve the origin coordinate singularity issue [15, 51, 60].

Although the FEM matrix entries must be numerically computed, as discussed in Remark 3.1, the computational cost to find the entries is optimal, scaling as $O(N_h N_p^2)$. Moreover, for coefficients that are not piecewise constant, the entries must also be numerically approximated in the case of a p-FEM $\otimes$ Fourier discretization.

3 Orthogonal Polynomials

In the previous section, we noted that our goal is to construct an FEM basis that promotes sparsity in the stiffness and mass matrices. In Section 4 we show that a suitable basis consists of so-called hat and bubble functions, otherwise known as external and internal shape functions, respectively. In this section we introduce the multivariate orthogonal polynomials that are used to define the hat and bubble functions.

3.1 Jacobi and Semiclassical Jacobi Polynomials

At its core, the hat and bubble functions consist of scaled-and-shifted (semi)classical Jacobi polynomials multiplied with harmonic polynomials. The (orthonormal) Jacobi polynomials $\{P_n^{(a,b)}(x)\}_{n\in\mathbb{N}_0}$ are a family of complete univariate bases of classical orthonormal polynomials on the interval $(-1, 1)$ with basis parameters $a, b \in \mathbb{R}$ such that $a, b > -1$ [39, Sec. 18.3]. They are orthonormal with respect to the L^2-weighted inner product

$$\int_{-1}^{1} P_n^{(a,b)}(x) P_m^{(a,b)}(x)\,(1-x)^a(1+x)^b \mathrm{d}x = \delta_{nm}. \tag{3.1}$$

A number of common orthogonal polynomials are special cases of Jacobi polynomials, e.g. Chebyshev and ultraspherical polynomials. A *weighted* orthogonal polynomial refers to an orthogonal polynomial multiplied by its orthogonality weight, e.g. the weighted Jacobi polynomials are $W_n^{(a,b)}(x) := (1-x)^a(1+x)^b P_n^{(a,b)}(x)$.

Semiclassical Jacobi orthogonal polynomials $\{Q_n^{t,(a,b,c)}(x)\}_{n\in\mathbb{N}_0}$ are a shifted generalization of the Jacobi polynomials. These are univariate orthogonal polynomials with respect to the inner product

$$\int_{0}^{1} Q_n^{t,(a,b,c)}(x) Q_m^{t,(a,b,c)}(x)\, x^a(1-x)^b(t-x)^c \mathrm{d}x = \delta_{nm}, \tag{3.2}$$

where $t > 1$, $a, b > -1$, and $c \in \mathbb{R}$. They were introduced by Magnus [35, Sec. 5] and are a building block for a variety of methods. When $c = 0$, these become scaled-and-shifted Jacobi polynomials and we drop the t dependence. That is, we have for any $t > 1$,

$$Q_n^{t,(a,b,0)}(x) = 2^{(a+b)/2} P_n^{(a,b)}(1-2x). \tag{3.3}$$

As with all univariate orthogonal polynomials, a three term recurrence exists for the generation of the (semiclassical) Jacobi polynomials. Equivalently, there exist tridiagonal Jacobi matrices, denoted by $X_{(a,b)}$ and $X_{t,(a,b,c)}$, such that

$$x\mathbf{P}^{(a,b)}(x) = \mathbf{P}^{(a,b)}(x) X_{(a,b)}, \quad x\mathbf{Q}^{t,(a,b,c)}(x) = \mathbf{Q}^{t,(a,b,c)}(x) X_{t,(a,b,c)}, \tag{3.4}$$

where $\mathbf{P}^{(a,b)}(x)$ and $\mathbf{Q}^{t,(a,b,c)}(x)$ denote the quasimatrix of the bases $\{P_n^{(a,b)}(x)\}_{n\in\mathbb{N}_0}$ and $\{Q_n^{t,(a,b,c)}(x)\}_{n\in\mathbb{N}_0}$, respectively.

The following lemma concerning the integral of the (semiclassical) Jacobi weights is used in the construction of the stiffness matrix of the hierarchical basis introduced in Section 4.

Lemma 3.1 *(Normalization) For $a, b > -1$, $c \in \mathbb{R}$, and $t > 1$,*

$$p_{(a,b)} := \int_{-1}^{1} (1-x)^a (1+x)^b \,\mathrm{d}x = 2^{a+b+1}\beta(a+1, b+1), \tag{3.5}$$

$$q_{t,(a,b,c)} := \int_{0}^{1} x^a (1-x)^b (t-x)^c \,\mathrm{d}x = t^c \beta(1+a, 1+b)\,{}_2F_1\left(\begin{matrix}1+a, -c\\ 2+a+b\end{matrix}; 1/t\right), \tag{3.6}$$

where β is the Beta function [39, Sec. 5.12] and ${}_2F_1$ is the Gauss hypergeometric function [39, Sec. 15.2].

3.2 Generalized Zernike and Zernike Annular Polynomials

We denote the generalized Zernike polynomials by $Z^{(a)}_{n,m,j}(x, y)$. These are two-dimensional multivariate orthogonal polynomials in the Cartesian coordinates (x, y) defined on the unit disk. Here a is the Zernike weight parameter for the orthogonality weight, n denotes the polynomial degree, m denotes the Fourier mode, and j denotes the Fourier sign. For n odd, $m \in \{1, 3, \ldots, n\}$, and for n even, $m \in \{0, 2, \ldots, n\}$. If $m = 0$ then $j = 1$, otherwise $j \in \{0, 1\}$. Throughout this work, we denote the polar coordinates by (r, θ) where $r^2 = x^2 + y^2$ and $\theta = \operatorname{atan}(y/x)$. We define the generalized Zernike polynomials as

$$Z^{(a)}_{n,m,j}(x, y) := Y_{m,j}(x, y) P^{(a,m)}_{(n-m)/2}(2r^2 - 1), \tag{3.7}$$

where

$$Y_{m,j}(x, y) := r^m \times \begin{cases} \cos(m\theta) & \text{if } m \in \mathbb{N}_0 \text{ and } j = 1, \\ \sin(m\theta) & \text{if } m \in \mathbb{N} \text{ and } j = 0, \end{cases} \tag{3.8}$$

are the harmonic polynomials, orthogonal on the surface of the disk. The generalized Zernike polynomials satisfy

$$\iint_{\Omega_0} Z^{(a)}_{n,m,j}(x, y) Z^{(a)}_{\nu,\mu,\zeta}(x, y)(1-r^2)^a \mathrm{d}x\mathrm{d}y = \frac{\pi_m}{2^{m+a+2}} \delta_{n\nu}\delta_{m\mu}\delta_{j\zeta}, \tag{3.9}$$

where $\pi_m = 2\pi$ if $m = 0$ and $\pi_m = \pi$ for $m \in \mathbb{N}$.

The generalized Zernike annular polynomials are the extension of the Zernike polynomials to the annulus domain and are used in the construction of gyroscopic polynomials [22]. They are denoted by $Z^{\rho,(a,b)}_{n,m,j}(x, y)$, where $0 < \rho < 1$, with the same relationship between n, m and j as for the Zernike polynomials. The non-generalized family (orthogonal with respect to the unweighted L^2-norm) was first introduced by Tatian [59] and Mahajan [36]. We define the generalized family as:

$$Z^{\rho,(a,b)}_{n,m,j}(x, y) := Y_{m,j}(x, y) Q^{t,(a,b,m)}_{(n-m)/2}\left(\frac{1-r^2}{1-\rho^2}\right). \tag{3.10}$$

Throughout this work we denote $\tau := t(1-r^2)$ where $t = (1-\rho^2)^{-1}$. Note that

$$1 - r^2 = t^{-1}\tau, \quad r^2 = t^{-1}(t-\tau), \quad \text{and} \quad r^2 - \rho^2 = t^{-1}(1-\tau). \tag{3.11}$$

Utilizing (3.11), one finds that $Z^{\rho,(a,b)}_{n,m,j}$ satisfy [51]

$$\iint_{\Omega_\rho} Z^{\rho,(a,b)}_{n,m,j}(x,y) Z^{\rho,(a,b)}_{\nu,\mu,\zeta}(x,y)(1-r^2)^a(r^2-\rho^2)^b \mathrm{d}x\mathrm{d}y = \frac{\pi_m}{2t^{a+b+m+1}}\delta_{n\nu}\delta_{m\mu}\delta_{j\zeta}. \tag{3.12}$$

Out of the spectral methods they considered for disks, Boyd and Yu [15] noted that Zernike polynomials often offer the best approximation per degree of freedom and a similar observation was made for the annulus [51, Sec. 6]. In order to compute with these polynomials quickly, we heavily rely on new methods for quasi-optimal $\mathcal{O}(N_p^2 \log N_p)$ complexity analysis (expansion) and synthesis (evaluation) operators introduced by Slevinsky [54] and Gutleb et al. [28] and further studied in [51, Sec. 4.2]. In a nutshell, for the analysis, one expands a function in a Chebyshev–Fourier series (for which a fast transform exists) and utilizes fast transforms to convert these expansion coefficients to those of the Zernike (annular) expansion. The synthesis operator is the reverse process.

As many operators decompose across Fourier modes, it is useful to consider each Fourier mode of the Zernike (annular) polynomials separately. Hence, we define the quasimatrix $\mathbf{Z}^{\rho,(a,b,c)}_{m,j}(x,y)$ as

$$\mathbf{Z}^{\rho,(a,b)}_{m,j}(x,y) := \left(Z^{\rho,(a,b)}_{m,m,j}(x,y) \mid Z^{\rho,(a,b)}_{m+2,m,j}(x,y) \mid Z^{\rho,(a,b)}_{m+4,m,j}(x,y) \mid \cdots \right). \tag{3.13}$$

The quasimatrix $\mathbf{Z}^{(a)}_{m,j}(x,y)$ is defined analogously.

3.3 Raising and Laplacian Matrices

In the next section, we will show that the (weighted) mass and stiffness matrices may be computed via the raising matrices for (semiclassical) Jacobi polynomials and the Laplacian matrices for Zernike (annular) polynomials.

Remark 3.1 (*Fast assembly*) In the next section, we will show how to compute the entries of the stiffness and mass matrices without any need for quadrature. Moreover, the entries of the load vector may also be computed in quasi-optimal complexity. This is achieved by considering hierarchies of raising matrices for (semiclassical) Jacobi polynomial families that can be computed in optimal complexity as detailed in [51, Sec. 4.1], see also [28, 54]. The right-hand side is expanded in Zernike annular polynomials by leveraging a fast DCT $\otimes$ FFT transform to compute the coefficients of a Chebyshev $\otimes$ Fourier expansion. These are then converted to the coefficients of a Zernike annular expansion via the hierarchy of raising matrices. How we then use the raising matrices to compute the entries of the FEM matrices and vectors is the main focus of Section 4.

Using raising matrices rather than quadrature to assemble the FEM matrices results in a fast and stable FEM framework.

We now define the hierarchy of raising matrices.

Definition 3.1 (*Raising matrices*) For $m \in \mathbb{N}_0$, we denote the raising matrix for weighted Jacobi and weighted semiclassical Jacobi polynomials by $R^{(0,m)}_{\mathrm{a},(1,m)}$ and $R^{t,(0,0,m)}_{\mathrm{ab},(1,1,m)}$, respectively, where

$$(1-x)\mathbf{P}^{(1,m)}(x) = \mathbf{P}^{(0,m)}(x) R^{(0,m)}_{\mathrm{a},(1,m)}, \tag{3.14}$$

$$x(1-x)\mathbf{Q}^{t,(1,1,m)}(x) = \mathbf{Q}^{t,(0,0,m)}(x)R^{t,(0,0,m)}_{\mathrm{ab},(1,1,m)}. \tag{3.15}$$

$R^{(0,m)}_{\mathrm{a},(1,m)}$ and $R^{t,(0,0,m)}_{\mathrm{ab},(1,1,m)}$ are lower triangular matrices with lower bandwidths one and two, respectively.

Recently a fast QR factorization technique was introduced that allows one to compute the semiclassical Jacobi hierarchy of raising matrices $\{R^{t,(0,0,m)}_{\mathrm{ab},(1,1,m)}\}_{m\in\{0,1,\ldots,N_p\}}$ in $\mathcal{O}(N_p^2)$ complexity [51, Sec. 3.1]. Thanks to explicit expressions for $R^{(0,m)}_{\mathrm{a},(1,m)}$, one may compute the Jacobi hierarchy in the same complexity.

Definition 3.2 (*Laplacian matrices*) For $m \in \mathbb{N}_0$, we denote the Laplacian matrix for weighted Zernike and weighted Zernike annular polynomials by D_m and D^{ρ}_m, respectively, where

$$\Delta[(1-r^2)\mathbf{Z}^{(1)}_{m,j}](x,y) = \mathbf{Z}^{(0)}_{m,j}(x,y)D_m, \tag{3.16}$$

$$\Delta[(1-r^2)(r^2-\rho^2)\mathbf{Z}^{(1,1)}_{m,j}](x,y) = \mathbf{Z}^{(0,0)}_{m,j}(x,y)D^{\rho}_m. \tag{3.17}$$

D_m and D^{ρ}_m are diagonal and tridiagonal matrices, respectively.

The same techniques that allow us to compute the raising matrices in optimal complexity, also allow us to compute the hierarchies of Laplacian matrices in optimal $\mathcal{O}(N_p^2)$ complexity [51, Sec. 3.4].

4 The FEM Basis: Hat and Bubble Functions

In this section we construct the hat and bubble functions that form the continuous hierarchical FEM basis Φ for disk and annulus domains.

Definition 4.1 (*Radial affine transformation*) Consider the disk and annular cells $K_0 = \Omega_{0,\rho}$, $\rho > 0$, $K_1 = \Omega_{\rho_1,\rho_2}$, $0 < \rho_1 < \rho_2$. Then we define the radial affine transformation of the Zernike (annular) polynomials as

$$\mathbf{Z}^{K_0,(a)}(x,y) := \mathbf{Z}^{(a)}\left(\frac{x}{\rho},\frac{y}{\rho}\right) \quad\text{and}\quad \mathbf{Z}^{K_1,(a,b)}(x,y) := \mathbf{Z}^{\rho_1/\rho_2,(a,b)}\left(\frac{x}{\rho_2},\frac{y}{\rho_2}\right). \tag{4.1}$$

Definition 4.2 (*Bubble functions*) Consider the disk and annular cells $K_0 = \Omega_{0,\rho}$, $\rho > 0$, and $K_1 = \Omega_{\rho_1,\rho_2}$, $0 < \rho_1 < \rho_2$. The disk and annulus bubble functions (otherwise known as internal shape functions) are denoted by $B^{K_0}_{n,m,j}(x,y)$ and $B^{K_1}_{n,m,j}(x,y)$, respectively, where

$$B^{K_0}_{n,m,j}(x,y) := (1-(r/\rho)^2)Z^{K_0,(1)}_{n,m,j}(x,y), \tag{4.2}$$

$$B^{K_1}_{n,m,j}(x,y) := (1-(r/\rho_2)^2)((r/\rho_2)^2-(\rho_1/\rho_2)^2)Z^{K_1,(1,1)}_{n,m,j}(x,y). \tag{4.3}$$

Note that the disk bubble functions vanish at $r = \rho$ and the annulus bubble functions vanish at $r = \rho_1$ and $r = \rho_2$.

We now distinguish between hat functions that are supported on two adjacent annulus elements and those supported on the disk element and the adjacent annulus element.

Definition 4.3 (*Disk-annulus hat functions*) Consider the disk and annular cells $K_0 = \Omega_{0,\rho_1}$ and $K_1 = \Omega_{\rho_1,\rho_2}, 0 < \rho_1 < \rho_2$. The disk-annulus hat functions (otherwise known as external shape functions) are defined as follows:

$$H_{m,j}^{K_0,K_1}(x,y) := \begin{cases} \kappa_m Z_{m,m,j}^{K_0,(0)}(x,y) & \text{in } K_0, \\ (1-(r/\rho_2)^2) Z_{m,m,j}^{K_1,(1,0)}(x,y) & \text{in } K_1. \end{cases}$$

The coefficient $\kappa_m := (1-(\rho_1/\rho_2)^2)(\rho_1/\rho_2)^m$ ensures the continuity of $H_{m,j}^{K_0,K_1}(x,y)$ at $r = \rho_1$.

The disk-annulus hat functions are only supported on the disk cell and the adjacent annular cell, vanishing at $r = \rho_2$.

Definition 4.4 (*Annulus-annulus hat functions*) Consider the annular cells $K_1 = \Omega_{\rho_1,\rho_2}$ and $K_2 = \Omega_{\rho_2,\rho_3}$, $0 < \rho_1 < \rho_2 < \rho_3$. The annulus-annulus hat functions (otherwise known as external shape functions) are defined as follows

$$H_{m,j}^{K_1,K_2}(x,y) := \begin{cases} \gamma_m((r/\rho_2)^2 - (\rho_1/\rho_2)^2) Z_{m,m,j}^{K_1,(0,1)}(x,y) & \text{in } K_1, \\ (1-(r/\rho_3)^2) Z_{m,m,j}^{K_2,(1,0)}(x,y) & \text{in } K_2. \end{cases}$$

The coefficient $\gamma_m := (1-(\rho_2/\rho_3)^2)(\rho_2/\rho_3)^m(1-(\rho_1/\rho_2)^2)^{-1}$ ensures the continuity of $H_{m,j}^{K_1,K_2}(x,y)$ at $r = \rho_2$.

The annulus-annulus hat functions are only supported on the two annular cells, vanishing at $r = \rho_1$ and $r = \rho_3$. In Fig. 3, we plot a one-dimensional slice at $\theta = 0$ of the bubble and hat functions with the Fourier mode and sign $(m, j) = (0, 1)$ and $(m, j) = (1, 1)$ on a two-cell mesh for increasing degree N_p. We emphasize that bubble functions are only ever supported on one cell and hat functions are supported on a maximum of two cells.

We denote the continuous hierarchical basis quasimatrix restricted to the Fourier mode (m, j) by $\mathbf{\Phi}_{m,j}$. We order the basis functions such that the basis functions of the same degree are grouped together. Hence, the hat functions across all the cells appear first and the bubble basis functions appear after. Consider the mesh $\mathcal{T}_h = \{\bar{K}_j\}_{j=0}^{N_h-1}$ where $K_j = \Omega_{\rho_j,\rho_{j+1}}$, $0 = \rho_0 < \rho_1 < \cdots < \rho_{N_h}$. Let

$$\mathbf{H}_{m,j}^{\mathcal{T}_h} := \begin{pmatrix} H_{m,j}^{K_0,K_1} & \cdots & H_{m,j}^{K_{N_h-2},K_{N_h-1}} & H_{m,j}^{K_{N_h-1},\bullet} \end{pmatrix} \quad (N_h \text{ hat functions}), \tag{4.4}$$

$$\mathbf{B}_{n,m,j}^{\mathcal{T}_h} := \begin{pmatrix} B_{n,m,j}^{K_0} & B_{n,m,j}^{K_1} & \cdots & B_{n,m,j}^{K_{N_h-1}} \end{pmatrix} \quad (N_h \text{ bubble functions per degree } n). \tag{4.5}$$

We use the superscript $^\bullet$ in a hat function that is only defined on one cell (such as the hat function at the boundary). $\mathbf{H}_{m,j}^{\mathcal{T}_h}(x,y)$ and $\mathbf{B}_{n,m,j}^{\mathcal{T}_h}(x,y)$ are the quasimatrices of the hat and bubble functions, respectively, on the mesh $\mathcal{T}_h$ restricted to the Fourier mode (m, j) and polynomial degree n. The hierarchical basis quasimatrix defined on the mesh $\mathcal{T}_h$, restricted to the Fourier mode (m, j) is

$$\mathbf{\Phi}_{m,j}^{\mathcal{T}_h} := \begin{pmatrix} \mathbf{H}_{m,j}^{\mathcal{T}_h} & \mathbf{B}_{m,m,j}^{\mathcal{T}_h} & \mathbf{B}_{m+2,m,j}^{\mathcal{T}_h} & \cdots \end{pmatrix}. \tag{4.6}$$

As is standard in FEM, we derive a number results for the local assembly of a matrix with respect to a reference element. The global assembly of the matrices is then deduced in the classical manner. With this in mind, we define the hierarchical basis quasimatrices on the unit disk domain Ω_0 and the annulus domain Ω_ρ as:

$$\mathbf{\Phi}_{m,j}^{\Omega_0}(x,y) := \begin{pmatrix} H_{m,j}^{\Omega_0,\bullet}(x,y) & B_{m,m,j}^{\Omega_0}(x,y) & B_{m+2,m,j}^{\Omega_0}(x,y) & \cdots \end{pmatrix}, \tag{4.7}$$

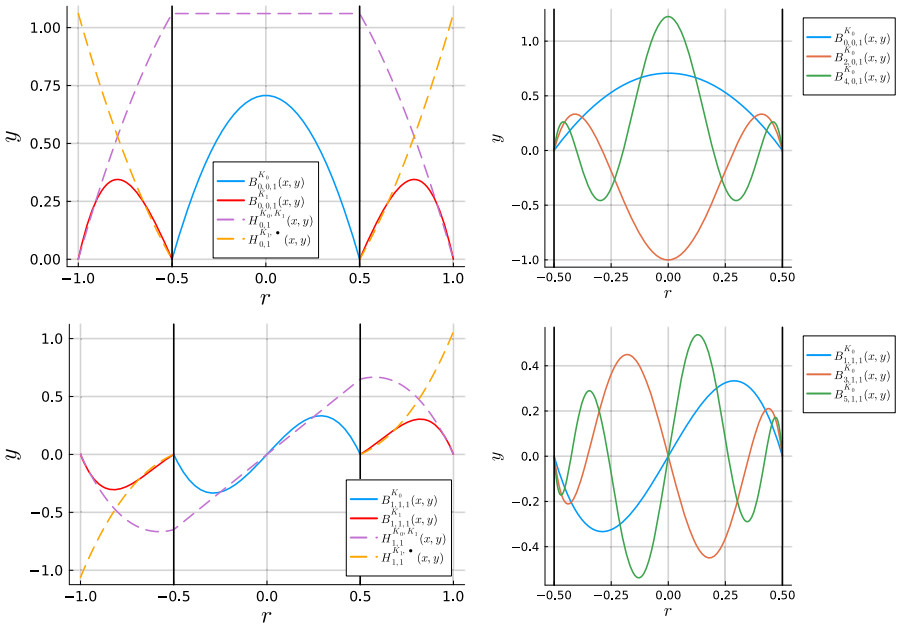

Fig. 3 Consider the mesh $\mathcal{T}_h = \{\bar{K}_0, \bar{K}_1\}$, $K_0 = \Omega_{0,1/2}$, $K_1 = \Omega_{1/2,1}$. (Left column) A one-dimensional slice at $\theta = 0$ is plotted for the hat and lowest degree bubble functions with the Fourier mode and sign $(m, j) = (0, 1)$ (top left) and $(m, j) = (1, 1)$ (bottom left) across the two cells. The solid black vertical lines indicate the edges of the cells. The bubble and hat functions are plotted with a solid and dashed line, respectively. (Right column) A one-dimensional slice at $\theta = 0$ of the first three bubble functions with $(m, j) = (0, 1)$ (top right) and $(m, j) = (1, 1)$ (bottom right) on the inner disk cell

$$\mathbf{\Phi}^{\Omega_\rho}_{m,j}(x, y) := \left(H^{\bullet,\Omega_\rho}_{m,j}(x, y)\ H^{\Omega_\rho,\bullet}_{m,j}(x, y)\ B^{\Omega_\rho}_{m,m,j}\ B^{\Omega_\rho}_{m+2,m,j}(x, y)\ \cdots\right), \tag{4.8}$$

$$\mathbf{\Phi}^{\Omega_0}(x, y) := \left(\mathbf{\Phi}^{\Omega_0}_{0,1}(x, y)\ \mathbf{\Phi}^{\Omega_0}_{1,0}(x, y)\ \mathbf{\Phi}^{\Omega_0}_{1,1}(x, y)\ \cdots\right), \tag{4.9}$$

$$\mathbf{\Phi}^{\Omega_\rho}(x, y) := \left(\mathbf{\Phi}^{\Omega_\rho}_{0,1}(x, y)\ \mathbf{\Phi}^{\Omega_\rho}_{1,0}(x, y)\ \mathbf{\Phi}^{\Omega_\rho}_{1,1}(x, y)\ \cdots\right). \tag{4.10}$$

For clarity, let $\mathbf{\Phi}^{\Omega}_{m,j}$ be the ith entry in (4.9) or (4.10), then $m = \lfloor i/2 \rfloor$ and $j = i \bmod 2$.

Remark 4.1 (*Homogeneous Dirichlet boundary condition*) A homogeneous Dirichlet boundary condition is enforced by dropping the hat functions in the basis that are nonzero on the boundary of the domain.

A crucial ingredient for constructing the (weighted) mass matrices in later sections will be the following proposition, which connects our basis to multivariate orthogonal polynomials with respect to a uniform weight:

Proposition 4.1 *(Raising operators) Consider the unit disk domain Ω_0 and the annulus domain Ω_ρ, $\rho > 0$. Recall the definitions of the raising matrices $R^{(0,m)}_{\mathrm{a},(1,m)}$ and $R^{t,(0,0,m)}_{\mathrm{ab},(1,1,m)}$ from Definition 3.1. Then*

$$\mathbf{\Phi}^{\Omega_0}_{m,j}(x, y) = \mathbf{Z}^{(0)}_{m,j}(x, y) R^{\Omega_0}_m \quad \textit{and} \quad \mathbf{\Phi}^{\Omega_\rho}_{m,j}(x, y) = \mathbf{Z}^{\rho,(0,0)}_{m,j}(x, y) R^{\Omega_\rho}_m, \tag{4.11}$$

where

$$R_m^{\Omega_0} := \left(\begin{array}{c|c} 1 & \\ 0 & \frac{1}{2}R^{(0,m)}_{\mathrm{a},(1,m)} \\ \vdots & \end{array}\right), \; R_m^{\Omega_\rho} := \frac{1}{t}\left(\begin{array}{cc|c} r_{11} & r_{12} & \\ r_{21} & r_{22} & \frac{1}{t}R^{t,(0,0,m)}_{\mathrm{ab},(1,1,m)} \\ 0 & 0 & \\ \vdots & \vdots & \end{array}\right), \tag{4.12}$$

such that $(r_{11} \quad r_{21} \quad \cdots)^\top$ *and* $(r_{12} \quad r_{22} \quad \cdots)^\top$ *are the first columns of the lower bidiagonal matrices* $R^{t,(0,0,m)}_{\mathrm{a},(1,0,m)}$ *and* $R^{t,(0,0,m)}_{\mathrm{b},(0,1,m)}$*, respectively, where* $x\mathbf{Q}^{t,(1,0,m)}(x) = \mathbf{Q}^{t,(0,0,m)}(x)R^{t,(0,0,m)}_{\mathrm{a},(1,0,m)}$ *and* $(1-x)\mathbf{Q}^{t,(0,1,m)}(x) = \mathbf{Q}^{t,(0,0,m)}(x)R^{t,(0,0,m)}_{\mathrm{b},(0,1,m)}$.

Proof We first consider the unit disk.
(Disk). Note that the first entries of $\mathbf{\Phi}^{\Omega_0}_{m,j}(x,y)$ and $\mathbf{Z}^{(0)}_{m,j}(x,y)$ are both $Z^{(0)}_{m,m,j}(x,y)$ which corresponds to the first column in $R_m^{\Omega_0}$. Now, for $\eta = 2r^2 - 1$,

$$\begin{aligned} \mathbf{B}^{\Omega_0}_{m,j}(x,y) &= \frac{1}{2}Y_{m,j}(x,y)(1-\eta)\mathbf{P}^{(1,m)}(\eta) \\ &= \frac{1}{2}Y_{m,j}(x,y)\mathbf{P}^{(0,m)}(\eta)R^{(0,m)}_{\mathrm{a},(1,m)} = \mathbf{Z}^{(0)}_{m,j}(x,y)\frac{1}{2}R^{(0,m)}_{\mathrm{a},(1,m)}. \end{aligned} \tag{4.13}$$

The first and third equalities follow from (3.7) and the second equality follows from Definition 3.1.
(Annulus). Note that $\mathbf{\Phi}^{\Omega_\rho}_{m,j} = \left(H^{\bullet,\Omega_\rho}_{m,j} \quad H^{\Omega_\rho,\bullet}_{m,j} \quad \mathbf{B}^{\Omega_\rho}_{m,j}\right)$. Now, for $\tau = t(1-r^2)$, $(x,y) \in \Omega_\rho$,

$$\begin{aligned} H^{\bullet,\Omega_\rho}_{m,j}(x,y) &= (1-r^2)Z^{\rho,(1,0)}_{m,j}(x,y) \\ &= t^{-1}Y_{m,j}(x,y)\tau Q_0^{t,(1,0,m)}(\tau) \\ &= t^{-1}Y_{m,j}(x,y)[r_{11}Q_0^{t,(0,0,m)}(\tau) + r_{21}Q_1^{t,(0,0,m)}(\tau)] \\ &= t^{-1}[r_{11}Z^{\rho,(0,0)}_{m,m,j}(x,y) + r_{21}Z^{\rho,(0,0)}_{m+2,m,j}(x,y)]. \end{aligned} \tag{4.14}$$

The first equality follows by the definition of the hat function, the second and fourth equalities follow from Definition 3.10 and the third equality follows from the definition of r_{11} and r_{12}. Thus we recover the first column and the second column follows similarly. We recover the remaining columns as follows:

$$\begin{aligned} \mathbf{B}^{\Omega_\rho}_{m,j}(x,y) &= (1-r^2)(r^2-\rho^2)Z^{\rho,(1,1)}_{m,j}(x,y) \\ &= t^{-2}Y_{m,j}(x,y)\tau(1-\tau)\mathbf{Q}^{t,(1,1,m)}(\tau) \\ &= t^{-2}Y_{m,j}(x,y)\mathbf{Q}^{t,(0,0,m)}(\tau)R^{t,(0,0,m)}_{\mathrm{ab},(1,1,m)} = t^{-2}\mathbf{Z}^{\rho,(0,0)}_{m,j}R^{t,(0,0,m)}_{\mathrm{ab},(1,1,m)}. \end{aligned} \tag{4.15}$$

□

Remark 4.2 $R_m^{\Omega_0}$ is upper triangular with upper bandwidth one and $R_m^{\Omega_\rho}$ is almost upper triangular (the upper-triangular structure is disrupted by the r_{21}-entry) with upper bandwidth two.

4.1 Mass and Stiffness Matrices

This subsection focuses on computing the entries of the mass and stiffness matrices. The entries are computed via the raising matrices defined in Proposition 4.1. In particular we emphasize that no quadrature is required.

Theorem 4.1 *(Mass matrix) Consider the unit disk domain Ω_0 and the annulus domain Ω_ρ, $\rho > 0$. Define the mass matrices $M^{\Omega_0} = \langle (\mathbf{\Phi}^{\Omega_0})^\top, \mathbf{\Phi}^{\Omega_0} \rangle_{L^2(\Omega_0)}$ and $M^{\Omega_\rho} = \langle (\mathbf{\Phi}^{\Omega_\rho})^\top, \mathbf{\Phi}^{\Omega_\rho} \rangle_{L^2(\Omega_\rho)}$. Then both M^{Ω_0} and M^{Ω_ρ} are block-diagonal where the blocks correspond to each Fourier mode:*

$$M^{\Omega_0} = \begin{pmatrix} M_{0,1}^{\Omega_0} & & & \\ & M_{1,0}^{\Omega_0} & & \\ & & M_{1,1}^{\Omega_0} & \\ & & & \ddots \end{pmatrix}, \quad M^{\Omega_\rho} = \begin{pmatrix} M_{0,1}^{\Omega_\rho} & & & \\ & M_{1,0}^{\Omega_\rho} & & \\ & & M_{1,1}^{\Omega_\rho} & \\ & & & \ddots \end{pmatrix} \tag{4.16}$$

where

$$M_{m,j}^{\Omega_0} = \langle (\mathbf{\Phi}_{m,j}^{\Omega_0})^\top, \mathbf{\Phi}_{m,j}^{\Omega_0} \rangle_{L^2(\Omega_0)} = \frac{\pi_m}{2^{m+2}} (R_m^{\Omega_0})^\top R_m^{\Omega_0}, \tag{4.17}$$

$$M_{m,j}^{\Omega_\rho} = \langle (\mathbf{\Phi}_{m,j}^{\Omega_\rho})^\top, \mathbf{\Phi}_{m,j}^{\Omega_\rho} \rangle_{L^2(\Omega_\rho)} = \frac{\pi_m}{2t^{m+1}} (R_m^{\Omega_\rho})^\top R_m^{\Omega_\rho}. \tag{4.18}$$

Thus $M_{m,0} = M_{m,1}$.

Proof If either $m \neq \mu$ or $j \neq \zeta$, then

$$\langle (\mathbf{\Phi}_{m,j}^{\Omega_0})^\top, \mathbf{\Phi}_{\mu,\zeta}^{\Omega_0} \rangle_{L^2(\Omega_0)} = \langle (\mathbf{\Phi}_{m,j}^{\Omega_\rho})^\top, \mathbf{\Phi}_{\mu,\zeta}^{\Omega_\rho} \rangle_{L^2(\Omega_\rho)} = \mathbf{0}, \tag{4.19}$$

where $\mathbf{0}$ denotes the infinite-dimensional matrix of zeroes. (4.19) follows by substituting in the definitions of the basis functions and noting that $\int_0^{2\pi} \sin(m\theta + j\pi/2) \sin(\mu\theta + \zeta\pi/2)\, \mathrm{d}\theta = 0$ if either $m \neq \mu$ or $j \neq \zeta$. In other words hat and bubble functions with different Fourier modes have a mass matrix entry of zero. This implies that the block diagonal structure in (4.16) holds.

For the disk cell, one finds that

$$\begin{aligned} M_{m,j}^{\Omega_0} &= \langle (\mathbf{\Phi}_{m,j}^{\Omega_0})^\top, \mathbf{\Phi}_{m,j}^{\Omega_0} \rangle_{L^2(\Omega_0)} = (R_m^{\Omega_0})^\top \langle (\mathbf{Z}_{m,j}^{(0)})^\top, \mathbf{Z}_{m,j}^{(0)} \rangle_{L^2(\Omega_0)} R_m^{\Omega_0} \\ &= \left(\int_0^{2\pi} \sin^2(m\theta + j\pi/2)\, \mathrm{d}\theta \right) \\ &\quad \times (R_m^{\Omega_0})^\top \langle (\mathbf{P}^{(0,m)})^\top, 2^{-(m+2)} (1+\eta)^m \mathbf{P}^{(0,m)} \rangle_{L^2(-1,1)} R_m^{\Omega_0} \\ &= 2^{-(m+2)} \pi_m (R_m^{\Omega_0})^\top R_m^{\Omega_0}. \end{aligned} \tag{4.20}$$

The first equality follows by the definition of the mass matrix and the second equality from Proposition 4.1. The third equality follows from (3.7) and a change from Cartesian coordinates (x, y) to polar coordinates (r, θ) followed a the second change of coordinates $\eta = 2r^2 - 1$. The final equality follows from a direct evaluation of the θ-dependent integral and the orthogonality of the Jacobi polynomials $\mathbf{P}^{(0,m)}$.

A similar calculation reveals that

$$\begin{aligned} M_{m,j}^{\Omega_\rho} &= \langle (\mathbf{\Phi}_{m,j}^{\Omega_\rho})^\top, \mathbf{\Phi}_{m,j}^{\Omega_\rho} \rangle_{L^2(\Omega_\rho)} = (R_m^{\Omega_\rho})^\top \langle (\mathbf{Z}_{m,j}^{\rho,(0,0)})^\top, \mathbf{Z}_{m,j}^{\rho,(0,0)} \rangle_{L^2(\Omega_\rho)} R_m^{\Omega_\rho} \\ &= \left(\int_0^{2\pi} \sin^2(m\theta + j\pi/2)\, \mathrm{d}\theta \right) \\ &\quad \times (R_m^{\Omega_\rho})^\top \langle (\mathbf{Q}^{t,(0,0,m)})^\top, 2^{-1} t^{-(m+1)} (t-\tau)^m \mathbf{Q}^{t,(0,0,m)} \rangle_{L^2(0,1)} R_m^{\Omega_\rho} \\ &= \frac{\pi_m}{2t^{m+1}} (R_m^{\Omega_\rho})^\top R_m^{\Omega_\rho}. \end{aligned} \tag{4.21}$$

□

Remark 4.3 $M^{\Omega_0}_{m,j}$ is tridiagonal and $M^{\Omega_\rho}_{m,j}$ has a 4×4 "arrowhead" followed by a pentadiagonal tail. Thus $M^{\Omega_\rho}_{m,j}$ is a B^3-Arrowhead matrix with block-bandwidths $(2, 2)$ and sub-block-bandwidth 1 [32, Def. 4.1]. Hence, the global mass matrix is block diagonal where each submatrix is a B^3-Arrowhead matrix with block-bandwidths $(2, 2)$ and sub-block-bandwidth 1.

Remark 4.4 Mass matrix entries corresponding to the L^2-inner product of bubble functions centred on different cells are equal to zero since their supports have zero measurable overlap.

The following lemma concerning the Laplacian applied to harmonic polynomial will be required to compute the entries of the stiffness matrix.

Lemma 4.1 *Let $\rho > 0$ and recall that $Y_{m,j}(x, y) := r^m \sin(m\theta + j\pi/2)$. Then the following holds:*

$$\Delta[(1 - r^2)Y_{m,j}] = -\Delta[(r^2 - \rho^2)Y_{m,j}] = -4(m + 1)Y_{m,j}. \tag{4.22}$$

Proof (4.22) follows by a direction calculation after applying the polar coordinate version of the Laplacian $\Delta = \partial^2_{rr} + \partial_r/r + \partial^2_{\theta\theta}/r^2$. □

Theorem 4.2 *(Stiffness matrix) Consider the unit disk domain Ω_0 and the annulus domain Ω_ρ, $\rho > 0$. Recall the definition of the Laplacian matrices D_m and D^ρ_m in Definition 3.2 and the normalization constants $p_{(a,b)}$ and $q_{t,(a,b,c)}$ from Lemma 3.1. Define the stiffness matrices $A^{\Omega_0} = \langle(\nabla\mathbf{\Phi}^{\Omega_0})^\top, \nabla\mathbf{\Phi}^{\Omega_0}\rangle_{L^2(\Omega_0)}$ and $A^{\Omega_\rho} = \langle(\nabla\mathbf{\Phi}^{\Omega_\rho})^\top, \nabla\mathbf{\Phi}^{\Omega_\rho}\rangle_{L^2(\Omega_\rho)}$. Then both A^{Ω_0} and A^{Ω_ρ} are block-diagonal where the blocks correspond to each Fourier mode:*

$$A^{\Omega_0} = \begin{pmatrix} A^{\Omega_0}_{0,1} & & & \\ & A^{\Omega_0}_{1,0} & & \\ & & A^{\Omega_0}_{1,1} & \\ & & & \ddots \end{pmatrix}, \quad A^{\Omega_\rho} = \begin{pmatrix} A^{\Omega_\rho}_{0,1} & & & \\ & A^{\Omega_\rho}_{1,0} & & \\ & & A^{\Omega_\rho}_{1,1} & \\ & & & \ddots \end{pmatrix} \tag{4.23}$$

where

$$A^{\Omega_0}_{m,j} = \langle(\nabla\mathbf{\Phi}^{\Omega_0}_{m,j})^\top, \nabla\mathbf{\Phi}^{\Omega_0}_{m,j}\rangle_{L^2(\Omega_0)} = \begin{pmatrix} \frac{m\pi}{p_{(0,m)}} & 0 \cdots \\ 0 & \\ \vdots & -\frac{\pi_m}{2^{m+3}} D_m \end{pmatrix}, \tag{4.24}$$

and

$$A^{\Omega_\rho}_{m,j} = \langle(\nabla\mathbf{\Phi}^{\Omega_\rho}_{m,j})^\top, \nabla\mathbf{\Phi}^{\Omega_\rho}_{m,j}\rangle_{L^2(\Omega_\rho)} = \begin{pmatrix} a_m & b_m & d_m & 0 \cdots \\ b_m & c_m & e_m & 0 \cdots \\ d_m & e_m & & \\ 0 & 0 & & -\frac{\pi_m}{2t^{m+3}} D^\rho_m \\ \vdots & \vdots & & \end{pmatrix}, \tag{4.25}$$

such that

$$a_m = \pi_m \frac{2 - \rho^{2m}(m(2 + m) - 2m(2 + m)\rho^2 + (2 - m(2 + m))\rho^4)}{(2 + m)q_{t,(1,0,m)}}, \tag{4.26}$$

$$b_m = -\frac{2\pi(1 - \rho^{4+2m})}{(2 + m)q^{1/2}_{t,(1,0,m)}q^{1/2}_{t,(0,1,m)}}, \tag{4.27}$$

$$c_m = \pi_m \frac{2 - 2\rho^{4+2m} + m(2+m)t^{-2}}{(2+m)q_{t,(0,1,m)}}, \tag{4.28}$$

$$d_m = 2\pi_m (m+1) q_{t,(1,1,m)}^{1/2} q_{t,(1,0,m)}^{-1/2} t^{-(m+3)}, \tag{4.29}$$

$$e_m = -2\pi_m (m+1) q_{t,(1,1,m)}^{1/2} q_{t,(0,1,m)}^{-1/2} t^{-(m+3)}. \tag{4.30}$$

Thus $A_{m,0} = A_{m,1}$.

Proof If either $m \neq \mu$ or $j \neq \zeta$, then

$$\langle (\nabla \mathbf{\Phi}_{m,j}^{\Omega_0})^\top, \nabla \mathbf{\Phi}_{\mu,\zeta}^{\Omega_0} \rangle_{L^2(\Omega_0)} = \langle (\nabla \mathbf{\Phi}_{m,j}^{\Omega_\rho})^\top, \nabla \mathbf{\Phi}_{\mu,\zeta}^{\Omega_\rho} \rangle_{L^2(\Omega_\rho)} = \mathbf{0}, \tag{4.31}$$

where $\mathbf{0}$ denotes the infinite-dimensional matrix of zeroes. (4.31) follows by substituting in the definitions of the basis functions and noting that $\int_0^{2\pi} \sin(m\theta + j\pi/2)\sin(\mu\theta + \zeta\pi/2)\,\mathrm{d}\theta = 0$ if either $m \neq \mu$ or $j \neq \zeta$. In other words hat and bubble functions with different Fourier modes have a stiffness matrix entry of zero. This implies that (4.23) holds.

First consider the disk cell.

(Disk). The (1,1) entry in (4.24) follows by a direct calculation:

$$\begin{aligned} \langle \nabla Z_{m,m,j}^{(0)}, \nabla Z_{m,m,j}^{(0)} \rangle_{L^2(\Omega_0)} &= p_{(0,m)}^{-1} \iint_{\Omega_0} \nabla Y_{m,j}(x,y) \cdot \nabla Y_{m,j}(x,y)\,\mathrm{d}x\mathrm{d}y \\ &= 2\pi m^2 p_{(0,m)}^{-1} \int_0^1 r^{2m-1}\,\mathrm{d}r = m\pi p_{(0,m)}^{-1}. \end{aligned} \tag{4.32}$$

The first equality follows from (3.7) and noting that $P_0^{(0,m)}(x) = p_{(0,m)}^{-1/2}$. The second equality follows by utilizing the gradient in polar coordinates, i.e. $\nabla = (\partial_r \quad \partial_\theta/r)^\top$ and a change from Cartesian coordinates to polar coordinates.

The remainder of $\mathbf{\Phi}_{m,j}^{\Omega_0}$ consists of bubble functions which vanish on the boundary of the cell. Thus one may perform an integration by parts and the boundary term vanishes, i.e.

$$\begin{aligned} \langle (\nabla \mathbf{B}_{m,j}^{\Omega_0})^\top, \nabla \mathbf{B}_{m,j}^{\Omega_0} \rangle_{L^2(\Omega_0)} &= -\langle (\mathbf{B}_{m,j}^{\Omega_0})^\top, \Delta \mathbf{B}_{m,j}^{\Omega_0} \rangle_{L^2(\Omega_0)} \\ &= -\langle (1-r^2)(\mathbf{Z}_{m,j}^{(1)})^\top, \mathbf{Z}_{m,j}^{(1)} \rangle_{L^2(\Omega_0)} D_m = -\frac{\pi_m}{2^{m+3}} D_m. \end{aligned} \tag{4.33}$$

The final equality follows from the orthogonality of $\mathbf{Z}_{m,j}^{(1)}$ where the normalization constant is calculated via the definition (3.7). It remains to show that the off-diagonal entries are zero. This follows as:

$$\begin{aligned} \langle \nabla Z_{m,m,j}^{(0)}, \nabla \mathbf{B}_{m,j}^{\Omega_0} \rangle_{L^2(\Omega_0)} &= -\langle \Delta Z_{m,m,j}^{(0)}, \mathbf{B}_{m,j}^{\Omega_0} \rangle_{L^2(\Omega_0)} \\ &= -p_{(0,m)}^{-1/2} \langle \Delta Y_{m,j}, \mathbf{B}_{m,j}^{\Omega_0} \rangle_{L^2(\Omega_0)} = 0. \end{aligned} \tag{4.34}$$

The final equality follows since, by definition, $\Delta Y_{m,j}(x,y) = 0$.

(Annulus). We first consider the interaction with the bubble functions with themselves. As the bubble functions vanish on the boundary of the element, one may perform an integration by parts and the boundary term vanishes. Hence,

$$\begin{aligned} &\langle (\nabla \mathbf{B}_{m,j}^{\Omega_\rho})^\top, \nabla \mathbf{B}_{m,j}^{\Omega_\rho} \rangle_{L^2(\Omega_\rho)} = -\langle (\mathbf{B}_{m,j}^{\Omega_\rho})^\top, \Delta \mathbf{B}_{m,j}^{\Omega_\rho} \rangle_{L^2(\Omega_\rho)} \\ &= -\langle (1-r^2)(r^2-\rho)^2 (\mathbf{Z}_{m,j}^{\rho,(1,1)})^\top, \mathbf{Z}_{m,j}^{\rho,(1,1)} \rangle_{L^2(\Omega_\rho)} D_m^\rho = -\frac{\pi_m}{2t^{m+3}} D_m^\rho. \end{aligned} \tag{4.35}$$

We now compute d_m in the (1,3)-entry and the trailing vector of zeroes from the (1,4)-entry in the first row. Note that these entries correspond to

$$\langle \nabla[(1-r^2)Z^{\rho,(1,0)}_{m,m,j}], \nabla \mathbf{B}^{\Omega_\rho}_{m,j}\rangle_{L^2(\Omega_\rho)} = -\langle \Delta[(1-r^2)Z^{\rho,(1,0)}_{m,m,j}], \mathbf{B}^{\Omega_\rho}_{m,j}\rangle_{L^2(\Omega_\rho)}, \tag{4.36}$$

where the equality follows by an integration by parts. Then, by utilizing Lemma 4.1 and definition (3.10), we see that

$$\begin{aligned} -\langle \Delta[(1-r^2)Z^{\rho,(1,0)}_{m,m,j}], \mathbf{B}^{\Omega_\rho}_{m,j}\rangle_{L^2(\Omega_\rho)} &= 4(m+1)\langle Z^{\rho,(1,0)}_{m,m,j}, \mathbf{B}^{\Omega_\rho}_{m,j}\rangle_{L^2(\Omega_\rho)} \\ &= 2\pi_m(m+1)t^{-(m+3)}\frac{q^{1/2}_{t,(1,1,m)}}{q^{1/2}_{t,(1,0,m)}} \\ &\quad \times \int_0^1 \tau(1-\tau)(t-\tau)^m Q_0^{t,(1,1,m)}(\tau)\mathbf{Q}^{t,(1,1,m)}(\tau)\,\mathrm{d}\tau \\ &= 2\pi_m(m+1)t^{-(m+3)}\frac{q^{1/2}_{t,(1,1,m)}}{q^{1/2}_{t,(1,0,m)}}\begin{pmatrix}1 & 0 & 0 & \cdots\end{pmatrix}. \end{aligned} \tag{4.37}$$

Thus we recover the value of d_m and the trailing zeroes. The value of e_m and the subsequent trail of zeroes in the second row follow in an almost identical fashion. It remains to verify the values of a_m, b_m, and c_m. Note that by Definition 3.10 and Lemma 4.1

$$\begin{aligned} a_m &= \langle \nabla[(1-r^2)Z^{\rho,(1,0)}_{m,m,j}], \nabla[(1-r^2)Z^{\rho,(1,0)}_{m,m,j}]\rangle_{L^2(\Omega_\rho)} \\ &= q^{-1}_{t,(1,0,m)}\langle \nabla[(1-r^2)Y_{m,j}], \nabla[(1-r^2)Y_{m,j}]\rangle_{L^2(\Omega_\rho)} \\ &= q^{-1}_{t,(1,0,m)}\iint_{\Omega_\rho} m^2(r^{2m-2}+r^{2m+2}) + (2m+1)r^{2m+2}\sin^2(m\theta + j\pi/2)\,\mathrm{d}x\mathrm{d}y \\ &= q^{-1}_{t,(1,0,m)}\left[2\pi\int_\rho^1 m^2(r^{2m-1}+r^{2m+3})\,\mathrm{d}r + \pi_m\int_\rho^1 (2m+1)r^{2m+3}\,\mathrm{d}r\right]. \end{aligned} \tag{4.38}$$

The third equality in (4.38) followed by utilizing the gradient in polar coordinates, i.e. $\nabla = (\partial_r \quad \partial_\theta/r)^\top$. The value of a_m follows by computing the final integral in (4.38). The values of b_m and c_m follow similarly. □

Remark 4.5 $A^{\Omega_0}_{m,j}$ is diagonal and $A^{\Omega_\rho}_{m,j}$ has a 3×3 "arrowhead" followed by a tridiagonal tail. Thus $A^{\Omega_\rho}_{m,j}$ is a B^3-Arrowhead matrix with block-bandwidths (1, 1) and sub-block-bandwidth 1 [32, Def. 4.1]. Hence, the global stiffness matrix is block diagonal where each submatrix is a B^3-Arrowhead matrix with block-bandwidths (1, 1) and sub-block-bandwidth 1.

4.2 Variable Helmholtz Coefficients

In this subsection we demonstrate how to handle variable coefficients.

4.2.1 Rotationally invariant coefficients

The hierarchical basis can discretize a rotationally invariant Helmholtz coefficient $\lambda(r^2)$ efficiently. Moreover, the sparsity of the induced weighted mass matrix M_λ is correlated with the number of terms in a Chebyshev expansion required to resolve the coefficient.

We first consider the following lemma:

Lemma 4.2 *Consider the disk and annular cells $K_0 = \Omega_{0,\rho}$, $\rho > 0$, $K_1 = \Omega_{\rho_1,\rho_2}$, $0 < \rho_1 < \rho_2$. Then*

$$r^2 \mathbf{Z}_{m,j}^{K_0,(a)}(x, y) = \frac{\rho^2}{2} \mathbf{Z}_{m,j}^{K_0,(a)}(x, y)(I + X_{(a,m)}), \tag{4.39}$$

$$r^2 \mathbf{Z}_{m,j}^{K_1,(a,b)}(x, y) = \rho_2^2 \mathbf{Z}_{m,j}^{K_1,(a,b)}(x, y)(I - t^{-1} X_{t,(a,b,m)}), \tag{4.40}$$

where I is the identity matrix.

Proof We prove (4.40) and note that (4.39) follows similarly. Consider $\tau = t(1 - r^2)$. Then, by utilizing (3.11),

$$\begin{aligned} r^2 \mathbf{Z}_{m,j}^{\rho,(a,b)}(x, y) &= r^2 Y_{m,j}(x, y) \mathbf{Q}^{t,(a,b,m)}(\tau) \\ &= Y_{m,j}(x, y)(1 - t^{-1}\tau) \mathbf{Q}^{t,(a,b,m)}(\tau) \\ &= Y_{m,j}(x, y) \mathbf{Q}^{t,(a,b,m)}(\tau)(I - t^{-1} X_{t,(a,b,m)}) \\ &= \mathbf{Z}_{m,j}^{\rho,(a,b)}(x, y)(I - t^{-1} X_{t,(a,b,m)}). \end{aligned} \tag{4.41}$$

Thus (4.40) holds when $\rho_1 = \rho$ and $\rho_2 = 1$. The result follows for a general annular cell K_1 with a scaling argument. □

Leveraging Lemma 4.2 we now describe how one discretizes a rotationally invariant Helmholtz coefficient $\lambda(r^2)$. The Helmholtz coefficient is expanded over each cell in the mesh independently.

Definition 4.5 We define $\{T_n\}_{n\in\mathbb{N}_0}$ as Chebyshev polynomials of the first kind [39, Sec. 18.3] and $T_n^{[a,b]}(x) := T_n((2x - a - b)/(b - a))$. In other words $\{T_n^{[a,b]}\}_{n\in\mathbb{N}_0}$ are Chebyshev polynomials of the first kind scaled to the interval $[a, b]$.

Theorem 4.3 *(Weighted mass matrix: disk) Consider the unit disk domain Ω_0 and let $\{T_n^{[0,1]}\}_{n\in\mathbb{N}_0}$ be the Chebyshev polynomials scaled to the interval $[0, 1]$ as defined in Definition 4.5.*

1. *Consider the expansion: $\lambda(r^2)|_{\Omega_0} = \sum_{n=0}^{\infty} \lambda_n T_n^{[0,1]}(r^2)$;*
2. *Let $\Lambda_m = \sum_{n=0}^{\infty} \lambda_n T_n^{[0,1]}((I + X_{(0,m)})/2)$.*

Then

$$\langle (\mathbf{\Phi}_{m,j}^{\Omega_0})^\top, \lambda(r^2) \mathbf{\Phi}_{m,j}^{\Omega_0} \rangle_{L^2(\Omega_0)} = \frac{\pi_m}{2^{m+2}} (R_m^{\Omega_0})^\top \Lambda_m R_m^{\Omega_0}. \tag{4.42}$$

Proof Note that

$$\begin{aligned} \langle (\mathbf{\Phi}_{m,j}^{\Omega_0})^\top, \lambda(r^2) \mathbf{\Phi}_{m,j}^{\Omega_0} \rangle_{L^2(\Omega_0)} &= (R_m^{\Omega_0})^\top \langle (\mathbf{Z}_{m,j}^{(0)})^\top, (\sum_{n=0}^{\infty} \lambda_n T_n^{[0,1]}(r^2)) \mathbf{Z}_{m,j}^{(0)} \rangle_{L^2(\Omega_0)} R_m^{\Omega_0} \\ &= (R_m^{\Omega_0})^\top \langle (\mathbf{Z}_{m,j}^{(0)})^\top \mathbf{Z}_{m,j}^{(0)} \rangle_{L^2(\Omega_0)} \Lambda_m R_m^{\Omega_0} = \frac{\pi_m}{2^{m+2}} (R_m^{\Omega_0})^\top \Lambda_m R_m^{\Omega_0}. \end{aligned} \tag{4.43}$$

The first equality holds thanks to Proposition 4.1 and the second equality holds thanks to Lemma 4.2. □

Theorem 4.4 *(Weighted mass matrix: annulus) Fix the annulus domain Ω_ρ, $\rho > 0$ and let $\{T_n^{[\rho,1]}\}_{n\in\mathbb{N}_0}$ be the Chebyshev polynomials scaled to the interval $[\rho, 1]$ as defined in Definition 4.5.*

1. *Consider the expansion:* $\lambda(r^2)|_{\Omega_\rho} = \sum_{n=0}^{\infty} \lambda_n T_n^{[\rho,1]}(r^2)$;
2. *Let* $\Lambda_m = \sum_{n=0}^{\infty} \lambda_n T_n^{[\rho,1]}(\rho^2(I - t^{-1}X_{t,(0,0,m)}))$.

Then

$$\langle (\mathbf{\Phi}_{m,j}^{\Omega_\rho})^\top, \lambda(r^2)(\mathbf{\Phi}_{m,j}^{\Omega_\rho})\rangle_{L^2(\Omega_\rho)} = \frac{\pi_m}{2t^{m+1}}(R_m^{\Omega_\rho})^\top \Lambda_m R_m^{\Omega_0}. \tag{4.44}$$

Proof The result follows analogously to the proof of Theorem 4.3 □

Remark 4.6 In practice we truncate the scaled Chebyshev expansion at some degree N and utilize the Clenshaw algorithm to compute the matrices Λ_m.

4.2.2 Rotationally anisotropic coefficients

If λ is rotationally anisotropic (it cannot be written as $\lambda(r)$) but it can be represented by a piecewise low-order polynomial in Cartesian coordinates, we may still recover a sparse discretization. However, a rotationally anisotropic coefficient means the PDE operator is now non-separable. In other words, the operator does not decouple across Fourier modes and thus the resulting linear system is not block diagonal.

We confine the discussion to discretizing $\lambda(x, y) = x$ on an annular cell. Discretizing on a disk cell follows similarly. For a more complex coefficient, one expands $\lambda(x, y)$ in a tensor-product Chebyshev expansion in x and y and the linear system is assembled akin to Section 4.2.1.

We first partially quote a proposition from [51].

Proposition 4.2 *(Proposition 4.8 in [51], x-Jacobi matrix) Let* $t = (1 - \rho^2)^{-1}$ *and* $R_{(a,b,c)}^{t,(a,b,c+1)}$ *denote the raising matrix for the orthonormal semiclassical Jacobi families* $\mathbf{Q}^{t,(a,b,c)} = \mathbf{Q}^{t,(a,b,c+1)} R_{(a,b,c)}^{t,(a,b,c+1)}$. *Then*

$$x\mathbf{Z}_{0,1}^{\rho,(a,b)}(x, y) = \mathbf{Z}_{1,1}^{\rho,(a,b)}(x, y) R_{(a,b,0)}^{t,(a,b,1)}, \tag{4.45}$$

$$x\mathbf{Z}_{1,0}^{\rho,(a,b)}(x, y) = \frac{1}{2}\mathbf{Z}_{2,0}^{\rho,(a,b)}(x, y) R_{(a,b,1)}^{t,(a,b,2)}, \tag{4.46}$$

and for, $m \geq 1$, $(m, j) \neq (1, 0)$,

$$x\mathbf{Z}_{m,j}^{\rho,(a,b)}(x, y) = \frac{1}{2}\left[t^{-1}\mathbf{Z}_{m-1,j}^{\rho,(a,b)}(x, y)(R_{(a,b,m-1)}^{t,(a,b,m)})^\top + \mathbf{Z}_{m+1,j}^{\rho,(a,b)}(x, y) R_{(a,b,m)}^{t,(a,b,m+1)}\right]. \tag{4.47}$$

Inspired by Proposition 4.2, we define the x-Jacobi matrix X^{Ω_ρ} as

$$X^{\Omega_\rho} = \begin{pmatrix} & \frac{1}{2t}(R_{(0,0,0)}^{t,(0,0,1)})^\top & & \\ & & \frac{1}{2t}(R_{(0,0,1)}^{t,(0,0,2)})^\top & \\ R_{(0,0,0)}^{t,(0,0,1)} & & & \ddots \\ & \frac{1}{2}R_{(0,0,1)}^{t,(0,0,2)} & & \\ & & \ddots & \end{pmatrix} \tag{4.48}$$

such that

$$x\begin{pmatrix}\mathbf{Z}_{0,1}^{\rho,(0,0)} & \mathbf{Z}_{1,0}^{\rho,(0,0)} & \mathbf{Z}_{1,1}^{\rho,(0,0)} & \cdots\end{pmatrix} = \begin{pmatrix}\mathbf{Z}_{0,1}^{\rho,(0,0)} & \mathbf{Z}_{1,0}^{\rho,(0,0)} & \mathbf{Z}_{1,1}^{\rho,(0,0)} & \cdots\end{pmatrix} X^{\Omega_\rho}. \tag{4.49}$$

Proposition 4.3 *Let $R_m^{\Omega_\rho}$ denote the raising operators defined in Proposition 4.1. Define*

$$R^{\Omega_\rho} := \begin{pmatrix} R_0^{\Omega_\rho} & & \\ & R_1^{\Omega_\rho} & \\ & & \ddots \end{pmatrix}, \quad D^{\Omega_\rho} := \begin{pmatrix} \mathrm{diag}(\frac{\pi_m}{2^2}) & & \\ & \mathrm{diag}(\frac{\pi_m}{2^4}) & \\ & & \ddots \end{pmatrix}, \tag{4.50}$$

such that $\Phi^{\Omega_\rho}(x, y) = \mathbf{Z}^{\rho,(0,0)}(x, y)R^{\Omega_\rho}$ and $\langle(\mathbf{Z}^{\rho,(0,0)})^\top, \mathbf{Z}^{\rho,(0,0)}\rangle_{L^2(\Omega_\rho)} = D^{\Omega_\rho}$. Then

$$\langle(\Phi^{\Omega_\rho})^\top, x\Phi^{\Omega_\rho}\rangle_{L^2(\Omega_\rho)} = (R^{\Omega_\rho})^\top D^{\Omega_\rho} X^{\Omega_\rho} R^{\Omega_\rho}. \tag{4.51}$$

Proof We note that

$$\langle(\Phi^{\Omega_\rho})^\top, x\Phi^{\Omega_\rho}\rangle_{L^2(\Omega_\rho)} = (R^{\Omega_\rho})^\top \langle(\mathbf{Z}^{\rho,(0,0)})^\top, x\mathbf{Z}^{\rho,(0,0)}\rangle_{L^2(\Omega_\rho)} R^{\Omega_\rho} \tag{4.52}$$

$$= (R^{\Omega_\rho})^\top \langle(\mathbf{Z}^{\rho,(0,0)})^\top, \mathbf{Z}^{\rho,(0,0)}\rangle_{L^2(\Omega_\rho)} X^{\Omega_\rho} R^{\Omega_\rho} \tag{4.53}$$

$$= (R^{\Omega_\rho})^\top D^{\Omega_\rho} X^{\Omega_\rho} R^{\Omega_\rho}. \tag{4.54}$$

□

The result in Proposition 4.3 then allows us to assemble the FEM matrices associated with anisotropic coefficients as further demonstrated in Section 6.4.

4.3 The Load Vector

In order to construct the load vector $\mathbf{b}$ in (2.6), we are required to test the data against a test function $\langle f, v\rangle_{L^2(\Omega)}$ for all $v \in H_0^1(\Omega)$ where the test function has been expanded in the basis Φ. We choose to expand the right-hand side in the discontinuous Zernike (annular) polynomial basis orthogonal with respect to the Lebesgue measure, which can be achieved in quasi-optimal complexity. More precisely, consider the mesh $\mathcal{T}_h = \{\bar{K}_j\}_{j=0}^{N_h-1}$ where $K_j = \Omega_{\rho_j,\rho_{j+1}}$, $0 = \rho_0 < \rho_1 < \cdots < \rho_{N_h}$ and the quasimatrix:

$$\mathbf{\Psi}_{m,j}^{\mathcal{T}_h} := \left(\mathbf{Z}_{m,j}^{K_0,(0)} \ \mathbf{Z}_{m,j}^{K_1,(0,0)} \ \cdots \ \mathbf{Z}_{m,j}^{K_{N_h-1},(0,0)}\right), \tag{4.55}$$

such that $\mathbf{\Psi}^{\mathcal{T}_h} := \left(\mathbf{\Psi}_{0,1}^{\mathcal{T}_h} \ \mathbf{\Psi}_{1,0}^{\mathcal{T}_h} \cdots\right)$. Then we expand $f(x, y)$ in (2.3) as $f(x, y) = \mathbf{\Psi}^{\mathcal{T}_h}(x, y)\mathbf{f}$ and fix $\mathbf{b} = \langle(\mathbf{\Phi}^{\mathcal{T}_h})^\top, \mathbf{\Psi}^{\mathcal{T}_h}\rangle_{L^2(\Omega)}\mathbf{f}$. The entries in the matrix $G_{\Phi,\Psi} := \langle(\mathbf{\Phi}^{\mathcal{T}_h})^\top, \mathbf{\Psi}^{\mathcal{T}_h}\rangle_{L^2(\Omega)}$ may be computed thanks to the following proposition.

Proposition 4.4 *(Load vector) Consider the unit disk domain Ω_0 and the annulus domain Ω_ρ, $\rho > 0$. Entries in $G_{\Phi,\Psi}$ associated with basis functions on different cells in the mesh are zero. Similarly, if either $m \neq \mu$ or $j \neq \zeta$, then*

$$\langle(\mathbf{\Phi}_{m,j}^{\Omega_0})^\top, \mathbf{Z}_{\mu,\zeta}^{\Omega_0,(0)}\rangle_{L^2(\Omega_0)} = \langle(\mathbf{\Phi}_{m,j}^{\Omega_\rho})^\top, \mathbf{Z}_{\mu,\zeta}^{\Omega_\rho,(0,0)}\rangle_{L^2(\Omega_\rho)} = \mathbf{0}, \tag{4.56}$$

where $\mathbf{0}$ denotes the infinite-dimensional matrix of zeroes. Moreover,

$$\langle(\mathbf{\Phi}_{m,j}^{\Omega_0})^\top, \mathbf{Z}_{m,j}^{\Omega_0,(0)}\rangle_{L^2(\Omega_0)} = \frac{\pi_m}{2^{m+2}}(R_m^{\Omega_0})^\top, \tag{4.57}$$

$$\langle(\mathbf{\Phi}_{m,j}^{\Omega_\rho})^\top, \mathbf{Z}_{m,j}^{\Omega_\rho,(0,0)}\rangle_{L^2(\Omega_\rho)} = \frac{\pi_m}{2t^{m+1}}(R_m^{\Omega_\rho})^\top. \tag{4.58}$$

Proof The proof of this result is very similar to the proof of Theorem 4.1. □

Remark 4.7 A more naïve approach for computing the load vector expands $f(x, y)$ directly in the continuous hierarchical FEM basis Φ and does a matrix-vector product with the mass matrices in Theorem 4.1. However, if $f(x, y)$ has a radial discontinuity, then an expansion in a continuous basis will result in a poor approximation. Moreover, as discussed in Section 4.5, the analysis operator for the basis Φ is increasingly ill-conditioned as $m \to \infty$.

4.4 Truncation

Until this section, the discussion revolved around computing operators which are infinite-dimensional. Hence (2.3) was being approximated exactly. However, in order to ensure the computations are numerically tractable, we must discretize the operators by truncating the stiffness and (weighted) mass matrices as well as the load vector. Consider a mesh $\mathcal{T}_h$ for the disk domain Ω. The continuous hierarchical basis quasimatrix $\mathbf{\Phi}^{\mathcal{T}_h}$ consists of the Fourier mode restrictions such that

$$\mathbf{\Phi}^{\mathcal{T}_h} := \begin{pmatrix} \mathbf{\Phi}_{0,1}^{\mathcal{T}_h} & \mathbf{\Phi}_{1,0}^{\mathcal{T}_h} & \mathbf{\Phi}_{1,1}^{\mathcal{T}_h} & \cdots \end{pmatrix}, \tag{4.59}$$

where $\mathbf{\Phi}_{m,j}^{\mathcal{T}_h}$ is as defined in (4.6). We denote a *truncation* of the quasimatrix at degree N_p on each element by $\mathbf{\Phi}^{\mathcal{T}_h,N_p}$. Suppose that N_p is even. Then

$$\mathbf{\Phi}^{\mathcal{T}_h,N_p} := \begin{pmatrix} \mathbf{\Phi}_{0,1}^{\mathcal{T}_h,N_p} & \mathbf{\Phi}_{1,0}^{\mathcal{T}_h,N_p} & \mathbf{\Phi}_{1,1}^{\mathcal{T}_h,N_p} & \cdots & \mathbf{\Phi}_{N_p,0}^{\mathcal{T}_h,N_p} & \mathbf{\Phi}_{N_p,1}^{\mathcal{T}_h,N_p} \end{pmatrix}, \tag{4.60}$$

where $\mathbf{\Phi}_{m,j}^{\mathcal{T}_h,N_p}$ denotes the finite-dimensional quasimatrix with any polynomial with degree $n > N_p$ removed. Thus $\mathbf{\Phi}_{N_p,j}^{\mathcal{T}_h,N_p}$ and $\mathbf{\Phi}_{N_p-1,j}^{\mathcal{T}_h,N_p}$ have one entry and $\mathbf{\Phi}_{N_p-2,j}^{\mathcal{T}_h,N_p}$ and $\mathbf{\Phi}_{N_p-3,j}^{\mathcal{T}_h,N_p}$ have two entries. Moreover, for $m < N_p - 3$, then $\mathbf{\Phi}_{m,j}^{\mathcal{T}_h,N_p}$ has $N_h(N_p - m)/2 + 2$ entries if m is even and $N_h(N_p - 3 - m)/2 + 2$ entries if m is odd.

The truncated (weighted) mass and stiffness matrices are subsequently formed from the truncated quasimatrices. For instance

$$M^{\Phi,N_p} = \langle (\Phi^{\mathcal{T}_h,N_p})^\top, \Phi^{\mathcal{T}_h,N_p} \rangle_{L^2(\Omega)} = \begin{pmatrix} M_{0,1}^{\Phi,N_p} & & & \\ & M_{1,0}^{\Phi,N_p} & & \\ & & \ddots & \\ & & & M_{N_p,1}^{\Phi,N_p} \end{pmatrix}, \tag{4.61}$$

such that $M^{\Phi,N_p} \in \mathbb{R}^{N\times N}$ where $N = \frac{1}{2}(N_h N_p + 2)(N_p - 1) + 2$.

4.5 Synthesis

In order to inspect and plot the solutions, one requires a fast synthesis (evaluation) operator, i.e. given a vector $\mathbf{u}$, we wish to evaluate $\mathbf{\Phi}(x_i, y_j)\mathbf{u}$ for a (non-Cartesian) grid of points $\{(x_i, y_j)\}_{ij}$ in quasi-optimal complexity $\mathcal{O}(N_h N_p^2 \log N_p)$. We focus on applying the synthesis operator on a single annular cell Ω_ρ, but we note that this technique generalizes to multiple cells. In particular, the synthesis operator may be applied on each cell in the mesh independently and in parallel.

Suppose we wish to evaluate an expansion of $u(x, y) = \Phi^{\Omega_\rho}(x, y)\mathbf{u}$ on the Zernike annular grid. Then by leveraging Proposition 4.1, we may construct a raising operator matrix

R^{Ω_ρ} (consisting of the Fourier mode submatrices $R_m^{\Omega_\rho}$) such that

$$u(x, y) = \mathbf{\Phi}^{\Omega_\rho}(x, y)\mathbf{u} = \mathbf{Z}^{\rho,(0,0)}(x, y)R^{\Omega_\rho}\mathbf{u} = \mathbf{Z}^{\rho,(0,0)}(x, y)\tilde{\mathbf{u}}. \tag{4.62}$$

Then one applies the quasi-optimal synthesis operator that exists for $\mathbf{Z}^{\rho,(0,0)}$ with the coefficient vector $\tilde{\mathbf{u}}$ [28, 51]. A synthesis operator for the disk cell follows analogously.

Remark 4.8 The analysis operator is the reverse of the synthesis operator. Given a known function $f(x, y)$ on Ω_ρ, the goal is to find the coefficient vector $\mathbf{f}$, in quasi-optimal complexity, such that $f(x, y) = \mathbf{\Phi}^{\Omega_\rho}(x, y)\mathbf{f}$. The analysis operator may be deduced by first expanding $f(x, y) = \mathbf{Z}^{\rho,(0,0)}(x, y)\tilde{\mathbf{f}}$ and then inverting the raising operator matrix $\mathbf{R}_m^{\Omega_\rho}$ for each Fourier mode to deduce the corresponding coefficient vector for $\mathbf{\Phi}_{m,j}^{\Omega_\rho}$. However, we note that a square truncation $\mathbf{R}_m^{\Omega_\rho}$ becomes increasingly ill-conditioned as $m \to \infty$. Hence, we advise against directly expanding a known function in the continuous hierarchical basis. Indeed, this is typically never required. One only ever expands the right-hand side in the well-conditioned $\mathbf{Z}^{\rho,(0,0)}(x, y)$ basis and computes the load vector as in Section 4.3.

4.6 Optimal Complexity Factorization and Solves

As shown in Section 4.1 the mass, M, and stiffness, A, matrices are block diagonal where each submatrix on the diagonal corresponds to a different Fourier mode of the basis. Moreover, the sparsity pattern of the submatrices are that of a B^3-Arrowhead matrix [32, Def. 4.1]. Symmetric positive-definite B^3-Arrowhead matrices admit a reverse Cholesky factorization (a Cholesky factorization initialized from the bottom right corner of the matrix rather than the top left) with sparse factors with zero fill-in [32, Cor. 4.3]. Thanks to the sparsity of the reverse Cholesky factors, they may be computed and inverted in optimal linear complexity $\mathcal{O}(N_h(N_p - m))$ where the Fourier mode submatrix has size $\lfloor N_h(N_p - m)/2\rfloor \times \lfloor N_h(N_p - m)/2\rfloor$. The linear complexity Cholesky factorization may be applied to any positive-definite addition of the mass and stiffness matrix, e.g. $A + \kappa^2 M$ for any $\kappa \in \mathbb{R}$. For more details on the optimal complexity reverse Cholesky factorization for the matrices that arise here, we refer the reader to [32].

The linear system in (2.6) may be indefinite for more general choices of λ. In the examples considered in Section 6, we have reported some success with a UL factorization (with no pivoting) and the factors remain sparse and computable in linear complexity. We do not expect this to be stable for a general choice of the Helmholtz coefficient λ. A stable alternative is a QL factorization which, for fixed N_h, achieves linear complexity as $N_p \to \infty$ but it is currently unknown how to achieve linear complexity as $N_h \to \infty$ due to fill-in.

For the factorizations to accurately capture the inverses of the matrices in the linear systems, we require each submatrix on the block-diagonal to be sufficiently well-conditioned. The conditioning of A and M is largely influenced by the continuity coefficients κ_m and γ_m in Definitions 4.3 and 4.4 for the hat functions. These coefficients degrade the conditioning as $m \to \infty$. Consider a mesh $\mathcal{T}_h = \{\bar{K}_j\}_{j=0}^{N_h-1}$ where $K_j = \Omega_{\rho_j,\rho_{j+1}}$, $0 = \rho_0 < \rho_1 < \cdots < \rho_{N_h}$. Let $\text{ratio}(\mathcal{T}_h) = \min_{j\in\{1,\ldots,N_h-1\}} \rho_j/\rho_{j+1}$. Then the smallest singular value of the submatrices is roughly $\mathcal{O}(\text{ratio}(\mathcal{T}_h)^m)$. $\text{ratio}(\mathcal{T}_h)$ is a measure of the thickness of the annuli cells in the mesh. The smaller the diameter of the cells, the closer the value of $\text{ratio}(\mathcal{T}_h)$ is to one and the better the conditioning. Thus the conditioning is improved by *increasing* the number of cells in the mesh. Consider a maximum truncation degree of N_p. In practice, provided one picks a mesh such that $\text{ratio}(\mathcal{T}_h)^{N_p} > 10^{-8}$ (double 64-bit precision), then utilizing a robust

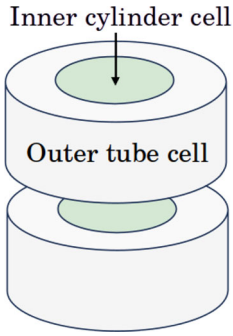

Fig. 4 A four cell mesh for the cylindrical domain $\mathbf{\Omega}$

factorization (such as reverse Cholesky or UL) means that the ill-conditioning will not cause numerical pollution in the solutions.

Remark 4.9 (*Static condensation*) The hierarchical ordering of the basis functions, together with the sparsity structure of the mass and stiffness matrices, mean that the induced Helmholtz linear systems are amenable to preconditioning via static condensation. Essentially one constructs the Schur complement induced by considering the top left block consisting of the rows and columns associated with the hat functions. Then the hat and bubble degrees of freedom may be solved for independently. For more details we refer the reader to [52, Ch. 3.2].

5 Quasi-Optimal Solves in 3D Cylindrical Domains

We construct a hierarchical FEM basis for a three-dimensional cylindrical domain with multiple elements not just in the x, y-axis but also the z-axis. This is achieved by considering the tensor-product space of the continuous FEM hierarchical basis for the disk with the univariate continuous hierarchical p-FEM basis for the interval as defined in [32, Sec. 2.1], see also [58, Ch. 2.5.2] and [52, Ch. 3.1]. Moreover, if the equation considered is the screened Poisson equation, then we prove that there exists a quasi-optimal $\mathcal{O}(N_h N_p^3 \log(N_h^{1/4} N_p))$ complexity solve. The setup complexity is $\mathcal{O}(N_h N_p^3 \log^2 N_p)$. To clarify, here we use N_p to denote the truncation degree of each polynomial basis factor of the tensor-product space, such that the tensor-product basis contains polynomials of maximum degree $2N_p$. N_h denotes the number of three-dimensional cells in the mesh. The total degrees of freedom is $\frac{1}{2}(N_h^{1/2} N_p + 2)(N_p - 1) + 2)((N_p + 1)N_h^{1/2} - 1) = \mathcal{O}(N_h N_p^3)$.

Without a loss of generality, let $\mathbf{\Omega} = \Omega_0 \times (-1, 1) \subset \mathbb{R}^3$ be a cylindrical domain. Let $\mathcal{T}_h$ denote a mesh for $\mathbf{\Omega}$ into cylindrical and tube cells as exemplified in Fig. 4.

Fix a Helmholtz coefficient $\lambda(r) \geq 0$ a.e. and consider the screened Poisson equation, find $u \in H_0^1(\Omega)$ that satisfies (2.3). We pick the basis $u(x, y, z) = \mathbf{\Phi}(x, y) U \mathbf{Q}(z)^\top$ where U is the matrix of expansion coefficients and $\mathbf{Q}(z)$ is the quasimatrix of the univariate continuous hierarchical p-FEM basis consisting of weighted Jacobi polynomials and piecewise linear hat functions defined in [32]. Note that $\mathbf{Q}(-1) = \mathbf{Q}(1) = \mathbf{0}$. In quasimatrix notation, the three-dimensional screened Poisson equation may be rewritten as a generalized Sylvester equation, i.e., find the coefficient matrix U that satisfies:

$$\left(M_\lambda^\Phi + A^\Phi\right) U M^Q + M^\Phi U A^Q = G_{\Phi,\Psi} F G_{Q,P}^\top. \tag{5.1}$$

Here M^Φ, M^Φ_λ, and A^Φ are the mass, weighted mass, and stiffness matrices, respectively, for the hierarchical basis Φ on the disk. Whereas M^Q and A^Q are the mass and stiffness matrices of the univariate basis. F denotes the matrix of expansion coefficients for the right-hand side $f(x, y, z) = \mathbf{\Psi}(x, y)F\mathbf{P}(z)^\top$ where $\mathbf{P}(z)$ denotes the quasimatrix of the discontinuous hierarchical basis (consisting of piecewise Legendre polynomials) [32]. Moreover, $G_{\Phi,\Psi} = \langle \mathbf{\Phi}^\top, \mathbf{\Psi}\rangle_{L^2(\Omega_0)}$ and $G_{Q,P} = \langle \mathbf{Q}, \mathbf{P}\rangle_{L^2(-1,1)}$. We note that A^Q, M^Q, and $G_{Q,P}$ are sparse [32]. Hence all the operator matrices appearing in (5.1) are sparse. We now truncate the tensor-product factor bases to degree N_p to recover the finite-dimensional matrices M^{Φ,N_p}_λ, M^{Φ,N_p}, A^{Φ,N_p}, A^{Q,N_p}, M^{Q,N_p}, $G^{N_p}_{\Phi,\Psi}$, and $G^{N_p}_{Q,P}$. For the remainder of this subsection, we drop the superscript N_p for readability.

The ADI algorithm is an iterative algorithm for finding the matrix X that solves the Sylvester equation $AX - XB = F$ [26]. It requires the two following assumptions to hold:

1. A and B are symmetric matrices;
2. There exist real disjoint nonempty intervals $[\mu_a, \mu_b]$ and $[\mu_c, \mu_d]$ such that $\sigma(A) \subset [\mu_a, \mu_b]$ and $\sigma(B) \subset [\mu_c, \mu_d]$, where σ denotes the spectrum of a matrix.

The algorithm proceeds iteratively. First one fixes the initial matrix $X_0 = 0$. Then, iteratively for $\ell \in \{1, 2, \ldots, \ell_{\max}\}$, we compute

$$X_{\ell-1/2} = (F - (A - p_\ell I)X_{\ell-1})(B - p_\ell I)^{-1}, \tag{5.2}$$

$$X_\ell = (A - q_\ell I)^{-1}(F - X_{\ell-1/2}(B - q_\ell I)), \tag{5.3}$$

where the value of the final iterate is $\ell_{\max} = \lceil \log(16\gamma)\log(4/\epsilon)/\pi^2 \rceil$ with $\gamma = |\mu_c - \mu_a||\mu_d - \mu_b|/(|\mu_c - \mu_b||\mu_d - \mu_a|)$. The ADI shifts p_ℓ and q_ℓ have explicit formulae depending on γ [26, Eq. (2.4)]. Notably, we have that $p_\ell > 0$ and $q_\ell < 0$ for all $\ell \in \{1, \ldots, \ell_{\max}\}$.

The first step to obtaining quasi-optimal solves is to notice that, due to the block diagonal (Fourier mode decoupling) nature of M^Φ and $M^\Phi_\lambda + A^\Phi$, (5.1) also admits a Fourier mode decoupling. Hence, for $m \in \{0, 1, \ldots, N_p\}$, $j \in \{0, 1\}$, $(m, j) \neq (0, 0)$, we instead consider the equations:

$$K^\Phi_{m,j} U_{m,j} M^Q + M^\Phi_{m,j} U_{m,j} A^Q = H_{m,j}, \tag{5.4}$$

where $K^\Phi_{m,j} := [M^\Phi_\lambda]_{m,j} + A^\Phi_{m,j}$ and $H_{m,j} := G_{\Phi_{m,j},\Psi_{m,j}} F_{m,j} G^\top_{Q,P}$. The following theorem reveals how to leverage the ADI algorithm to solve (5.4) for each Fourier mode.

Theorem 5.1 *Consider the cylindrical domain $\mathbf{\Omega} = \Omega_0 \times (-1, 1)$ and a mesh $\mathcal{T}_h$ as depicted in Fig. 4. Consider the reverse Cholesky factorizations of the truncated matrices (not indicated) $L^\top L = A^Q$ and $V^\top V = K^\Phi_{m,j}$.*

Suppose that $\sigma(L^{-\top} M^Q L^{-1}) \subset [\mu_a, \mu_b]$ and $\sigma(-V^{-\top} M^\Phi_{m,j} V^{-1}) \subset [\mu_c, \mu_d]$. Pick an ADI tolerance ϵ. Let $\gamma = |\mu_c - \mu_a||\mu_d - \mu_b|/(|\mu_c - \mu_b||\mu_d - \mu_a|)$ and fix $\ell_{\max} = \lceil \log(16\gamma)\log(4/\epsilon)/\pi^2 \rceil$. Assign $W_0 = \mathbf{0}$ and for $\ell \in \{1, 2, \ldots, \ell_{\max}\}$ compute:

$$W_{\ell-1/2} = [H_{m,j} - (M^\Phi_{m,j} - p_\ell K^\Phi_{m,j})W_{\ell-1}](-M^Q - p_\ell A^Q)^{-1} \tag{5.5}$$

$$W_\ell = (M^\Phi_{m,j} - q_\ell K^\Phi_{m,j})^{-1}[H_{m,j} - W_{\ell-1/2}(-M^Q - q_\ell A^Q)], \tag{5.6}$$

Then $U_{m,j} \approx W_{\ell_{\max}}(A^Q)^{-1}$. More precisely,

$$\|V(U_{m,j} - W_{\ell_{\max}}(A^Q)^{-1})L^\top\|_2 \le \epsilon \|V U_{m,j} L^\top\|_2. \tag{5.7}$$

Proof The result follows by a direct application of Lemma 5.1 in [32]. □

Thanks to Theorem 5.1, we may compute $U_{m,j}$ via the ADI algorithm. The remainder of this sections focuses on showing that the solution may be computed in quasi-optimal $\mathcal{O}(N_h N_p^3 \log(N_h^{1/2} N_p) \log \epsilon^{-1})$ flops. The first step is to show that asymptotically $\ell_{\max} = \mathcal{O}(\log(N_h^{1/2} N_p) \log \epsilon^{-1})$.

Lemma 5.1 *(Inverse inequality) Consider a disk or annulus domain $\Omega_{a,b}$, $0 \leq a < b$. Suppose that π_p denotes a degree p multivariate polynomial. Let $h = b - a$. Then there exists a $c > 0$ such that the following inverse inequality holds:*

$$\|\nabla \pi_p\|_{L^2(\Omega_{a,b})} \leq c h^{-1} p^2 \|\pi_p\|_{L^2(\Omega_{a,b})}. \tag{5.8}$$

Proof The case of a disk domain, $a = 0$, was shown in [19, Ex. 4.25]. Then the extension to the annulus domain follows by leveraging a rescaling argument in the radial direction akin to the techniques introduced in [16, Ch. 4.5]. □

Proposition 5.1 *(Spectrum) Suppose the conditions of Theorem 5.1 hold and $\lambda \in L^\infty(\Omega)$ with $\lambda(r) \geq 0$ a.e. in Ω. Suppose the mesh is quasi-uniform such that $N_h \sim h^{-2}$, where h denotes the minimum diameter of the cells in the mesh [16, Def. 4.4.13]. Consider the reverse Cholesky factorizations of the truncated matrices (not indicated) $L^\top L = A^Q$ and $V^\top V = K^\Phi_{m,j}$. Then there exist constants $0 < c \leq C < \infty$, independent of N_p and N_h, such that*

$$\sigma(L^{-\top} M^Q L^{-1}) \subseteq \left[\frac{1}{12 N_h N_p^4}, \frac{4}{\pi^2}\right], \tag{5.9}$$

$$\sigma(V^{-\top} M^\Phi_{m,j} V^{-1}) \subseteq [c(N_h N_p^4 + \|\lambda\|_{L^\infty(\Omega)})^{-1}, C]. \tag{5.10}$$

It follows that asymptotically $\ell_{\max} = \mathcal{O}(\log(N_h^{1/4} N_p) \log \epsilon^{-1})$ where $\ell_{\max}$ is the value of final iterate in the ADI algorithm and ϵ is the ADI tolerance.

Proof (5.9) was shown to hold in [32, Lem. 5.2] and (5.10) may be derived by utilizing Lemma 5.1 and following the proof of [32, Lem. 5.2] with some small modifications. □

Corollary 5.1 *Suppose the conditions of Proposition 5.1 hold. Then (5.1) may be solved with $\mathcal{O}(N_h N_p^3 \log(N_h^{1/4} N_p) \log \epsilon^{-1})$ flops via the ADI algorithm, where ϵ is the ADI tolerance for each Fourier mode subsolve.*

Proof We first note that the eigenvalues μ_a and μ_b may be approximated in $\mathcal{O}(N_h^{1/2} N_p)$ flops via an inverse iteration (with shifts). The same is true for μ_c and μ_d but in $\mathcal{O}(N_h^{1/2} N_p^2)$ flops. The result then follows by deconstructing each component of the setup and execution of the ADI algorithm in Theorem 5.1. The most expensive part of the algorithm is the $\ell_{\max}$ solves of (5.5) and (5.6) for each Fourier mode. Thanks to the optimal complexity reverse Cholesky factorization discussed in Section 4.6, we have that each solve requires $\mathcal{O}(N_h N_p^2)$ flops. Proposition 5.1 reveals that $\mathcal{O}(\ell_{\max}) = \mathcal{O}(\log(N_h^{1/4} N_p) \log \epsilon^{-1})$. Thus the $\ell_{\max}$ solves requires $\mathcal{O}(N_h N_p^2 \log(N_h^{1/4} N_p) \log \epsilon^{-1})$ flops. This must be conducted over $\mathcal{O}(N_p)$ Fourier modes resulting in an $\mathcal{O}(N_h N_p^3 \log(N_h^{1/4} N_p) \log \epsilon^{-1})$ complexity solve. □

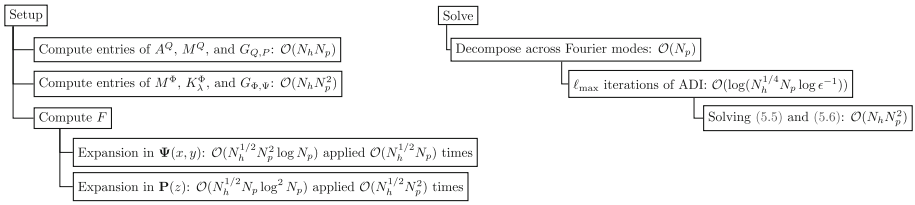

Fig. 5 Complexity flowchart of the setup and solve for the 3D screened Poisson equation of Section 6.6. The overall complexity of the setup is $\mathcal{O}(N_h N_p^3 \log^2 N_p)$ and the solve is $\mathcal{O}(N_h N_p^3 \log(N_h^{1/4} N_p) \log \epsilon^{-1})$

6 Examples

In this section we utilize the hierarchical FEM basis introduced in this paper for disk and annulus domains to approximately solve a number of equations. When measuring the errors, we measure the ℓ^∞-norm on a heavily over-resolved Zernike (annular) grid on each cell in the mesh.

6.1 Plane Wave with Discontinuous Coefficients and Data

The first example we consider is a plane wave problem with radial discontinuities in both the right-hand side $f(x, y)$ and the Helmholtz coefficient $\lambda(r)$. Consider $\rho, \lambda_0, \lambda_1 > 0$ and define:

$$\tilde{u}(r) = \frac{1}{4} \times \begin{cases} \lambda_0 r^2 + (\lambda_1 - \lambda_0)\rho^2 - \lambda_1 + 2(\lambda_0 - \lambda_1)\rho^2 \log(\rho) & \text{if } 0 \le r \le \rho, \\ \lambda_1 r^2 - \lambda_1 + 2(\lambda_0 - \lambda_1)\rho^2 \log(r) & \text{if } \rho < r \le 1. \end{cases} \tag{6.1}$$

In this example we choose the Helmholtz coefficient:

$$\lambda(r) = \Delta \tilde{u}(r) = \begin{cases} \lambda_0 & \text{if } 0 \le r \le \rho, \\ \lambda_1 & \text{if } \rho < r \le 1. \end{cases} \tag{6.2}$$

Note that $\tilde{u}(r)$ is twice differentiable (but the second derivative is not continuous) and $\tilde{u}(1) = 0$. Consider a unit disk domain Ω_0 and fix the parameters as $\rho = 1/2$, $\lambda_0 = 10^{-2}$, $\lambda_1 = 50$. Let $u_e(x, y) = \sin(50x)\tilde{u}(r)$ and consider the right-hand side $f(x, y) = [-\frac{1}{50}\Delta + \lambda(r)]u_e(x, y)$. Our goal is to recover the exact known solution $u_e(x, y)$ by approximately finding $u \in H_0^1(\Omega_0)$ that satisfies the screened Poisson equation:

$$\frac{1}{50}\langle \nabla v, \nabla u \rangle_{L^2(\Omega_0)} + \langle v, \lambda u \rangle_{L^2(\Omega_0)} = \langle v, f \rangle_{L^2(\Omega_0)}. \tag{6.3}$$

We mesh the unit disk domain with $\mathcal{T}_h = \{0 \le r \le 1/2\} \cup \{2^{-(j+1)/9} \le r \le 2^{-j/9}\}_{j \in \{0,1,\ldots,9\}}$ culminating in $N_h = 10$ cells. We then compute the load vector from $f(x, y)$ as described in Section 4.3 and compute the stiffness and weighted mass matrices as described in Sections 4.1 and 4.2.1. The resultant matrix is block diagonal where the blocks correspond to the Fourier mode decoupling and have a B^3-Arrowhead matrix structure. Hence, we solve for each block individually via a reverse Cholesky factorization (as described in Section 4.6) for an optimal complexity solve: $\mathcal{O}(N_h N_p^2)$.

We plot the right-hand side f and the approximated solution u of (6.3) on the whole domain Ω_0 as well as a slice at $\theta = 0.6168$ in Fig. 6. Note the discontinuity of the right-hand side at $r = 1/2$. We examine the convergence of the discretization with a fixed mesh

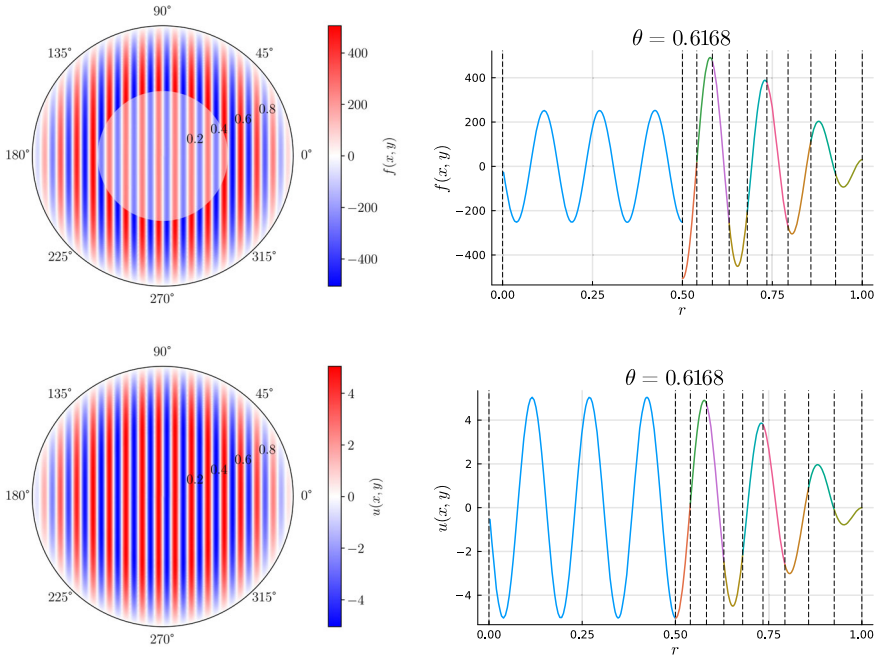

Fig. 6 Plots of the right-hand side $f(x, y)$ (top) and solution $u(x, y)$ (bottom) of the plane wave problem of Section 6.1. The black vertical lines in the slice plots indicate the edges of the cells in the mesh. The right-hand side has a radial discontinuity at $r = 1/2$. Nevertheless the sparse hp-FEM accurately captures the jump and enforces the necessary continuity in the solution

but as $N_p \to \infty$ in Fig. 7. After an initial plateau, we observe spectral convergence as we simultaneously increase N_p on each element.

6.2 High Frequency with a Discontinuous Helmholtz Coefficient

In this example we consider the indefinite Helmholtz equation (2.3) on the unit disk domain Ω_0. We pick a Helmholtz coefficient and a right-hand side with radial discontinuities at $r = 1/2$:

$$\lambda(r) = \begin{cases} -80^2 & \text{if } 0 \le r \le 1/2, \\ -90^2 & \text{if } 1/2 < r \le 1, \end{cases} \quad \text{and} \quad f(x, y) = \begin{cases} 2\sin(200x) & \text{if } 0 \le r \le 1/2, \\ \sin(100y) & \text{if } 1/2 < r \le 1. \end{cases} \tag{6.4}$$

We mesh the unit disk domain with $\mathcal{T}_h = \{0 \le r \le 1/2\} \cup \{2^{-(j+1)/11} \le r \le 2^{-j/11}\}_{j\in\{0,1,\ldots,11\}}$ culminating in $N_h = 12$ cells. We compute the entries of the matrices in the indefinite linear system (2.6) as in the previous example. The resultant matrix is block diagonal where the blocks correspond to the Fourier mode decoupling. We solve for each block individually via a UL factorization with no pivoting for an optimal complexity solve: $\mathcal{O}(N_h N_p^2)$. We provide the spy plots of the $(m, j) = (175, 1)$ Fourier mode submatrix of $A + M_\lambda$ and the UL factors in Fig. 8 when $N_p = 200$.

We do not have a closed-form expression for the exact solution of this problem. Hence, we measure the error against two over-resolved reference solutions. The first reference solution

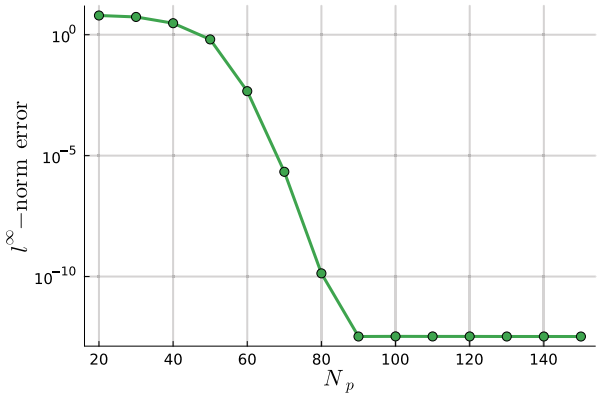

Fig. 7 A semi-log convergence plot of the ℓ^∞-norm error of the hierarchical basis for the plane wave problem of Section 6.1 with increasing polynomial degree N_p on each of the 10 cells in the mesh. The plot indicates spectral convergence when $N_p > 50$ despite the radial discontinuities in $\lambda(r)$ and $f(x, y)$.

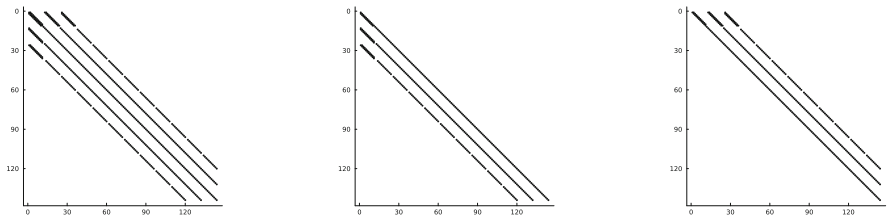

(a) $(m, j) = (175, 1)$ submatrix (b) reverse L factor (c) reverse U factor

Fig. 8 Spy plots of the $(m, j) = (175, 1)$ Fourier mode submatrix of $A + M_\lambda$ and its UL factors (computed without pivoting) that arise in Section 6.2. The mesh contains 12 cells and the polynomial order is $N_p = 200$ on each element. The UL factors are sparse, have no fill-in, and may be computed in linear complexity

is computed via the sparse hp-FEM of this work. The second reference solution is computed via the SEM introduced in [51, Sec. 6] which discretizes the strong form of the equation. In this reference solution, the domain is meshed into the two cells $\Omega_0 = \Omega_{0,1/2} \cup \Omega_{1/2,1}$. A Zernike polynomial discretization is used in the inner disk cell and a Chebyshev–Fourier series discretization is used in the outer annular cell. Boundary conditions and continuity across the cells are enforced via a tau-method [51, Sec. 6], see also [18, 47].

We plot the right-hand side f and the approximated solution u on the whole domain Ω_0 as well as a slice at $\theta = 0.6319$ in Fig. 9. The negative Helmholtz coefficient causes oscillations to occur in the solution which are normally very difficult to capture. Moreover, one can spot the change in the behaviour of the solution as one crosses the radial discontinuity barrier at $r = 1/2$. We plot the convergence of the sparse hp-FEM in Fig. 10. After an initial period where the error decreases slowly, we observe spectral convergence for $N_p > 100$. Convergence is reached at $N_p = 160$. The error with respect to the reference SEM solution stagnates at $\mathcal{O}(10^{-12})$ with is due to the discretization error in the reference solution.

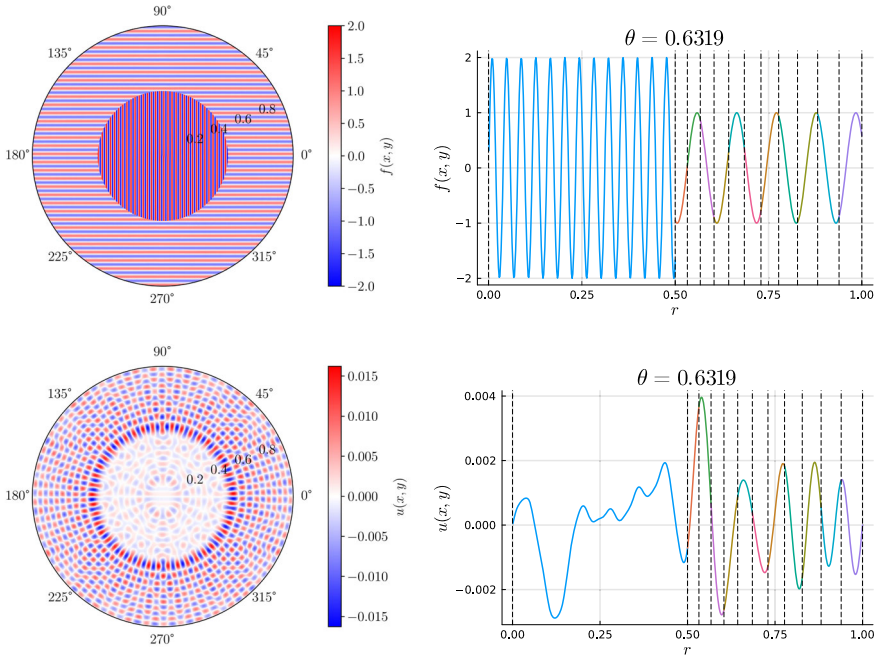

Fig. 9 Plots of the right-hand side $f(x, y)$ (top) and solution $u(x, y)$ (bottom) of the high frequency problem in Section 6.2 with the Helmholtz coefficient and right-hand side as given in (6.4). The black vertical lines in the slice plots indicate the edges of the cells in the mesh. The right-hand side and Helmholtz coefficient have a radial discontinuity at $r = 1/2$. Nevertheless the sparse hp-FEM accurately captures the jump and enforces the necessary continuity in the solution

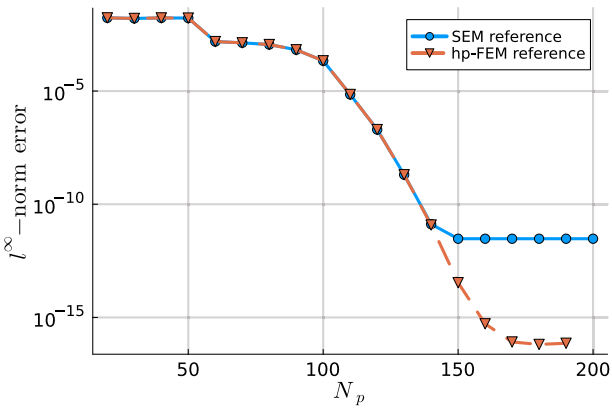

Fig. 10 A semi-log convergence plot of the ℓ^{∞}-norm error of the continuous hierarchical basis for the high frequency problem in Section 6.2 with increasing polynomial degree N_p on each of the 12 cells in the mesh. After an initial plateau until $N_p = 100$, the plot indicates spectral convergence despite the radial discontinuities in the problem data and the high-frequency oscillations of the solution. The larger error plateau with respect to the reference SEM solution is due to the discretization error in the reference solution

6.3 Time-Dependent Schrödinger Equation

The time-dependent Schrödinger equation is one of the fundamental equations in quantum mechanics and describes how the wave function of a quantum system changes in response to the energy of the system. We consider the following form of the equation:

$$\mathrm{i}\hbar\partial_t u(x,y,t) = \left(-\frac{\hbar^2}{2m}\Delta + V(r^2)\right)u(x,y,t), \quad u(x,y,0) = u^{(0)}(x,y), \tag{6.5}$$

where $t > 0$ and $(x, y) \in \mathbb{R}^2$. Here i is the imaginary unit, $\mathrm{i}^2 = -1$, $\hbar$ is the reduced Planck constant, m is the mass of the particle, and V is the potential of the environment. We assume V depends on r^2 and is stationary. From here on, we choose the normalization constants $\hbar = 1$, $m = 1/2$ and let $\lambda(r^2) = V(r^2)$. Thus (6.5) reduces to

$$\mathrm{i}\partial_t u(x,y,t) = \left(-\Delta + \lambda(r^2)\right)u(x,y,t), \quad u(x,y,0) = u^{(0)}(x,y). \tag{6.6}$$

(6.6) is unitary and has the solution $u(x, y, t) = \mathrm{e}^{-\mathrm{i}t(-\Delta+\lambda)}u^{(0)}(x, y)$ which implies that

$$\|u(\cdot,\cdot,t)\|_{L^2(\mathbb{R}^2)} = \|u^{(0)}\|_{L^2(\mathbb{R}^2)} \quad \text{for any} \quad t > 0. \tag{6.7}$$

A favourable property for any temporal discretization of (6.6) is that the energy is conserved, i.e. (6.7) holds. Provided the spatial discretization leads to a symmetric linear system, then the Crank–Nicolson method is the simplest temporal discretization that preserves energy and to which we restrict our investigations. High-order temporal discretizations will be considered in future work [9, 29].

Closed form expressions for the solutions of (6.6) are difficult to find. When $\lambda(r^2) = r^2$ in (6.6), the problem is known as the quantum harmonic oscillator. Here, the eigenfunctions of the operator $(-\Delta + r^2)$ are known and take the form [62, Eq. (17)]:

$$(-\Delta + r^2)\psi_{n,m}(x,y) = E_{n,m}\psi_{n,m}(x,y), \tag{6.8}$$

where $\psi_{n,m}(x, y) = H_n(x)H_m(y)\exp(-(x^2 + y^2)/2)$ and $E_{n,m} = 2(n + m + 1)$. Here H_n, $n \in \mathbb{N}_0$, denote the orthonormalized Hermite polynomials [39, Sec. 18.3]. Thus if $u^{(0)}(x, y) = \psi_{n,m}(x, y)$, then the solution of (6.6) is $u(x, y, t) = \mathrm{e}^{-\mathrm{i}E_{n,m}t}\psi_{n,m}(x, y)$.

As the domain in (6.6) is $\mathbb{R}^2$, we truncate the domain to the disk $\bar{\Omega} = \{0 \le r \le 50\}$. We mesh the domain with the 16 cells $\mathcal{T}_h = \{0 \le r \le 50(6/5)^{-15}\} \cup \bigcup_{j=0}^{14}\{50(6/5)^{j+1} \le r \le 50(6/5)^j\}$. We discretize (6.6) in the time variable with the Crank–Nicolson method with the uniform time step δt. We consider the final time $T = 2\pi/E_{20,21}$ which corresponds to one full period of oscillation of the solution, $u(x, y, T) = u(x, y, 0)$. Rewritten in quasimatrix form, then at each time step $k = 0, 1, 2, \ldots$, the time-stepping problem reduces to solving:

$$(2M + \mathrm{i}\delta t(A + M_{r^2}))\mathbf{u}^{(k+1)} = (2M - \mathrm{i}\delta t(A + M_{r^2}))\mathbf{u}^{(k)}. \tag{6.9}$$

We consider the initial state $u^{(0)}(x, y) = \psi_{20,21}(x, y)$. We discretize in space with the continuous hierarchical FEM basis with truncation degree $N_p = 100$ on each cell. This problem and discretization preserves the Fourier mode decoupling and, therefore, the matrices in (6.9) are block diagonal with $2N_p + 1$ blocks which may be decoupled into $2N_p + 1$ independent linear systems. Each block permits a complex-valued UL factorization with no pivoting. Moreover, the complex-valued UL factors may be computed in linear complexity and are sparse with zero fill-in as observed in Fig. 11.

The initial state is plotted in Fig. 12 and the spatial discretization yields an ℓ^∞-norm error of 7.94×10^{-15}. As discussed one must truncate the domain sufficiently large in order

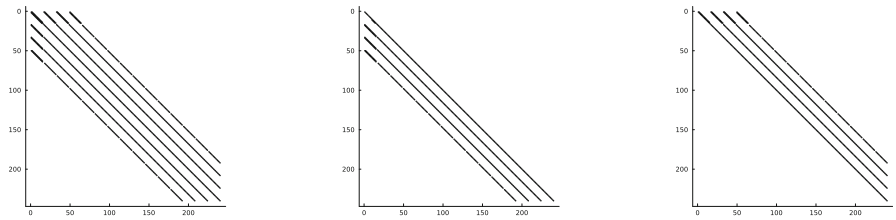

(a) $(m, j) = (70, 1)$ submatrix (b) reverse L factor (c) reverse U factor

Fig. 11 Absolute value spy plots of the $(m, j) = (70, 1)$ Fourier mode complex-valued submatrix of $2M + \mathrm{i}\delta t(A + M_{r^2})$ and the complex-valued UL factors (computed without pivoting) as they arise in Section 6.3. The mesh contains 16 cells and the polynomial order is $N_p = 100$ on each element. The UL factors are sparse, have no fill-in, and may be computed in linear complexity

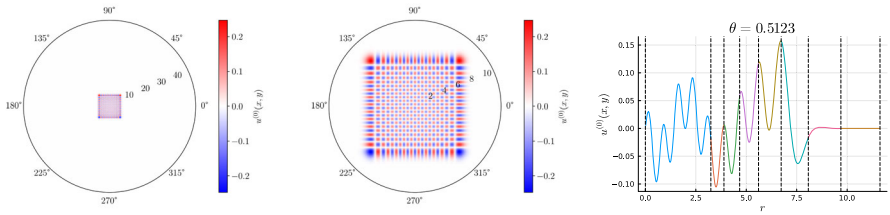

Fig. 12 Plots of the initial state $u^{(0)}(x, y)$ in the Schrödinger equation of Section 6.3 on the whole domain (left) and zoomed in (middle). A slice of the initial state in the first 8 cells is also displayed (right). The black vertical lines in the slice plot indicates the edges of the cells

to sufficiently emulate an unbounded domain. However, since the initial state exponentially decays as $r \to \infty$, the initial state evaluates to below (double) machine precision for $r > 9$. A one-cell discretization would struggle to sufficiently capture the oscillations of the initial state close to the origin. Our investigations revealed that a one-cell Zernike $\mathbf{Z}^{(0)}(x, y)$ discretization required a truncation degree $N_p = 700$ to resolve the initial state to an ℓ^∞-norm error of 5×10^{-15} on the domain $\Omega = \{0 \le r \le 50\}$.

A convergence plot is given in Fig. 13 for decreasing step size δt where we measure the ℓ^∞-norm error at the final time step $T = 2\pi/E_{20,21}$ (which always had the largest error across all the time steps). We observe the expected $\mathcal{O}(\delta t^2)$ convergence. Fig. 13 displays a plot of the difference in the $L^2(\Omega)$-norm between the approximate solution at time step iterate k and the discretization of the initial state for the finest temporal discretization where $\delta t = 5.75 \times 10^{-5}$. In other words we plot $|\|u^{(k)}\|_{L^2(\Omega)} - \|u^{(0)}\|_{L^2(\Omega)}|$ for $k = 1, 2, \ldots, 1300$. We see that there is some loss of energy due to the floating point error. At each time step $|\|u^{(k+1)}\|_{L^2(\Omega)} - \|u^{(k)}\|_{L^2(\Omega)}| \approx 10^{-13}$ and $1300 \times 10^{-13} \approx 10^{-10}$.

6.4 Rotationally Anisotropic Coefficient

Here we consider an equation with a Helmholtz coefficient that is rotationally anisotropic, i.e. λ cannot be written as $\lambda(r)$. Let $\Omega = \{10^{-2} < r < 1\}$. We seek $u \in H_0^1(\Omega)$ that satisfies

$$(-\Delta - 80^2 x)u(x, y) = \begin{cases} (1 + \mathrm{e}^{-12x}) \sin(50x) & \text{if } 10^{-2} \le r < 1/2, \\ (1 + \mathrm{e}^{-6x}) \sin(50y) & \text{if } 1/2 \le r \le 1. \end{cases} \tag{6.10}$$

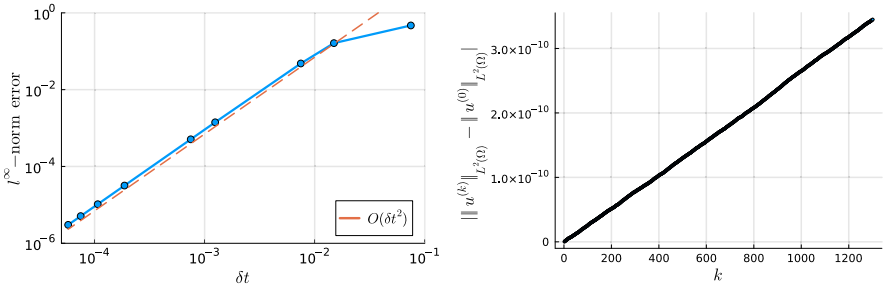

Fig. 13 (Left) A log-log convergence plot of the ℓ^∞-norm error at the final time step $T = 2\pi/E_{20,21}$ as $\delta t \to 0$ for the time-dependent Schrödinger equation described in Section 6.3. The domain is a disk with outer radius 50. It is meshed into 16 cells where we truncate at $N_p = 100$ on each element. The plot indicates the expected $\mathcal{O}(\delta t^2)$ convergence of the Crank–Nicolson temporal discretization. (Right) The difference in the $L^2(\Omega)$-norm between a time step iterate and the discretization of the initial state when $\delta t = 5.75 \times 10^{-5}$

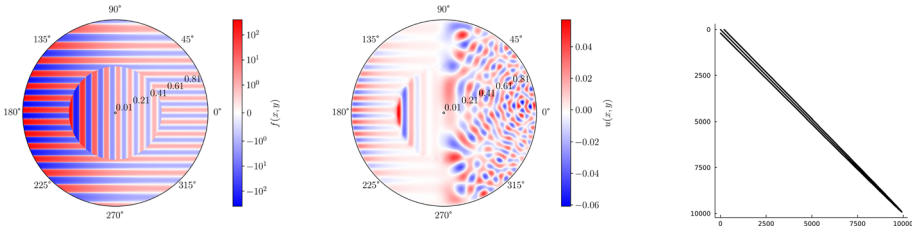

Fig. 14 Plots of the right-hand side (left) and the solution (middle) in the non-separable problem of Section 6.4 with the right-hand side and rotationally anisotropic Helmholtz coefficient as given in (6.10). We mesh the domain into two cells meeting at $r = 1/2$ which corresponds with the radial discontinuity of the right-hand side. As x grows from -1 to 1, we notice a change in the behaviour of the solution corresponding to the transition of a solution to the screened Poisson equation to one of a Helmholtz problem. On the right, we provide a spy plot of the FEM discretization matrix of (6.10) where $N_p = 100$ on both cells

By leveraging the x-Jacobi matrix for Zernike annular polynomials (as discussed in Section 4.2.2), we are able to assemble the FEM linear system efficiently. Moreover, since the coefficient is a polynomial of degree one, we retain sparsity. However, the PDE operator is no longer rotationally invariant and the resulting discretization matrix is not block diagonal unlike the previous examples. We mesh the domain into two annular cells at $\{10^{-2} \leq r \leq 1/2\}$ and $\{1/2 \leq r \leq 1\}$ which align with the radial discontinuity of the right-hand side. We then consider a discretization degree of $N_p = 100$ on both cells, assemble the linear system and solve it via a sparse LU factorization. In Fig. 14 we provide a spy plot of the FEM matrix as well as plots of the right-hand side and the solution. Note that when $x < 0$, the PDE operator is locally positive-definite but when $x > 0$, we enter a Helmholtz regime. This is reflected in the solution where we notice a switch in the behaviour at $x = 0$ from structured oscillations to highly unstructured oscillations akin to those in the solution of the high frequency problem in Section 6.2.

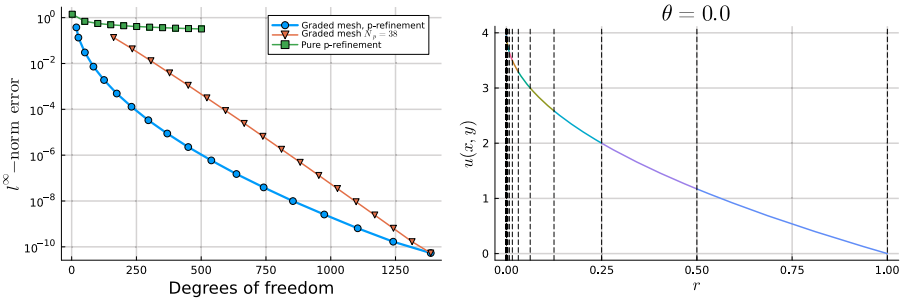

Fig. 15 (Left) Convergence to the solution u of (6.11) via a pure p-refinement on a single-celled mesh and via a graded mesh with a fixed truncation degree $N_p = 38$ (graded mesh, $N_p = 38$) or where $N_p = N$ (graded mesh, p-refinement). The errors are measured against the number of degrees of freedom in the solution coefficient vector of the first Fourier mode $(m, j) = (0, 1)$. The convergence of the second strategy is spectral. (Right) A one-dimensional slice of the approximate solution at $N = 38$, i.e. where $N_h = 77$ and $N_p = 38$. The dashed vertical lines indicate the edges of the annular cells which are graded towards the origin

6.5 Singular Source Term

In this example we consider the unit disk domain $\Omega_0 = \{r < 1\}$ and seek $u \in H_0^1(\Omega_0)$ that satisfies

$$-\Delta u = r^{-3/2}. \tag{6.11}$$

The exact solution to (6.11) is $u(x, y) = 4 - 4(x^2 + y^2)^{1/4} = 4 - 4r^{1/2}$. This problem features a non-integrable singularity at $r = 0$ in the source term as well as a square-root singularity in the solution. These singularity will impede the convergence of a p-refinement strategy. Nevertheless, we will recover spectral convergence to the solution by constructing a mesh that is graded towards the origin [52, Ch. 3].

In Fig. 15 we consider three discretization strategies. One involves fixing a single-celled mesh (the unit disk) and solely increasing the truncation degree N_p (pure p-refinement). Due to the singularity, p-refinement is ineffective. Consequentially, even when $N_p = 1004$ (corresponding to 502 degrees of freedom in the first Fourier mode coefficient) we still observe an ℓ^∞-norm error of 0.32. The other two strategies involve constructing a mesh of the unit disk domain where $\mathcal{T}_N = \{0 \le r \le 2^{-2N}\} \cup \{2^{-n} \le r \le 2^{-(n-1)}\}_{n \in \{1,2,3,\ldots,2N\}}$. This results in a mesh with $N_h = 2N + 1$ cells which are graded towards the origin. Then, for each mesh $\mathcal{T}_N$ we consider either an FEM discretization with degree $N_p = N$ on each cell (graded mesh, p-refinement) or fix $N_p = 38$ across all the meshes (graded mesh, $N_p = 38$). The latter strategy recovers spectral convergence to the exact solution with respect to number of degrees of freedom in the solution coefficient vector of the first Fourier mode $(m, j) = (0, 1)$. Note that due to the rotational symmetry of the solution, the solution coefficients corresponding to other Fourier modes are equal zero. The former strategy achieves a smaller error per degree of freedom. However the convergence is not spectral. In Fig. 15 we also provide a one-dimensional slice of the approximate solution when $N = N_p = 38$ at $\theta = 0$. The vertical dashed lines indicate the edges of the annular cells in the mesh.

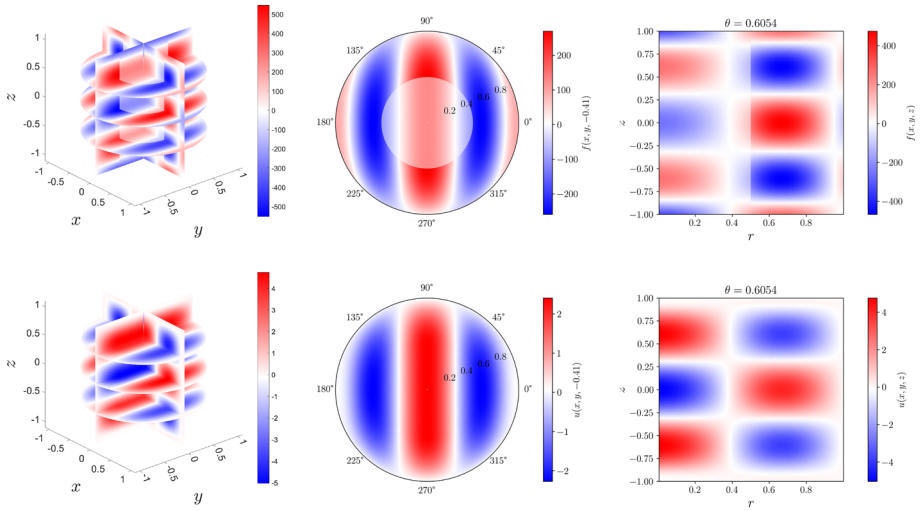

Fig. 16 Plots of the right-hand side $f(x, y, z)$ (top row) and the solution $u(x, y, z)$ (bottom row) in the 3D cylinder screened Poisson equation of Section 6.6 with the right-hand side and Helmholtz coefficient as given in (6.12). The first column is a visualization on the 3D domain, the second column is a 2D slice in the (x, y)-plane and final column is a 2D slice through the z-plane

6.6 Screened Poisson in a 3D Cylinder

In this example we solve the screened Poisson on a 3D cylinder with a quasi-optimal complexity setup and solve of $\mathcal{O}(N_h N_p^3 \log^2 N_p)$ and $\mathcal{O}(N_h N_p^3 \log^2 N_h^{1/4} N_p)$, respectively. We utilize the hierarchical tensor-product FEM basis designed in Section 5. Recall that in 3D we use N_p to denote the truncation degree of each polynomial basis factor of the tensor-product space, such that the tensor-product basis contains polynomials of maximum degree $2N_p$. N_h denotes the number of three-dimensional cells in the mesh.

Let $\mathbf{\Omega} = \Omega_0 \times (-1, 1) \subset \mathbb{R}^3$ be a cylindrical domain. Consider the screened Poisson equation, find $u \in H_0^1(\mathbf{\Omega})$ that satisfies (2.3) and choose the Helmholtz coefficient and the right-hand side:

$$\lambda(r) = \begin{cases} 10^{-2} & \text{if } 0 \le r \le 1/2, \\ 50 & \text{if } 1/2 < r \le 1, \end{cases} \quad \text{and} \quad f(x, y, z) = (-\Delta + \lambda(r))u_e(x, y, z), \tag{6.12}$$

where $u_e(x, y, z) = \cos(5x)\tilde{u}(r)\cos(5z)(1 - z^6)$. We pick $\tilde{u}(r)$ as defined in (6.1) with $\lambda_0 = 10^{-2}, \lambda_1 = 50$, and $\rho = 1/2$. We mesh the domain into four cells: $\{r \le 1/2\} \times [-1, 0]$, $\{r \le 1/2\} \times [0, 1]$, $\{1/2 \le r \le 1\} \times [-1, 0]$, and $\{1/2 \le r \le 1\} \times [0, 1]$. In Fig. 16, we plot the right-hand side and the solution together with slices in (x, y) and z plane. Note the radial discontinuity in the right-hand side. The convergence plot is displayed in Fig. 17. We observe spectral convergence of our discretization as we increase N_p in each cell. In Fig. 17 we also plot the growth of final ADI iteration $\ell_{\max}$,, as $N_p \to \infty$, averaged over all the Fourier mode solves (5.4) in order to solve the full problem (5.1). We observe the expected lograthmic growth.

To exemplify the flexibility of the hierarchical basis on the cylinder, in Fig. 2 we plot the right-hand side and solution to a screened Poisson equation with a radial discontinuous Helmholtz coefficient $\lambda(r^2)$ and a right-hand side $f(x, y, z)$ with discontinuities at $r = 1/2$

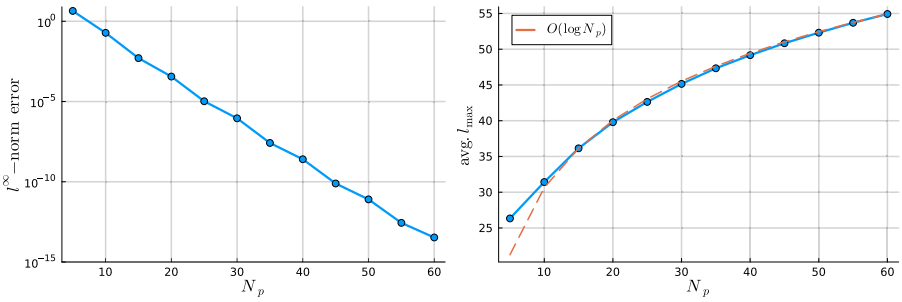

(a) ℓ^∞-norm error (b) Average value of $l_{\max}$

Fig. 17 (Left) A semi-log convergence plot of the ℓ^∞-norm error of the hp-FEM basis for the 3D cylinder screened Poisson problem in Section 6.6 with a right-hand side and Helmholtz coefficient as given in (6.12) with increasing polynomial degree N_p on each of the four cells in the mesh. The plot indicates spectral convergence despite the radial discontinuities in the problem data. (Right) The growth of the final ADI iterate value $\ell_{\max}$ as defined in Theorem 5.1 averaged across all the Fourier modes solves (5.4) for increasing N_p. We observe logarithmic growth

and $z = 0$. Let

$$\lambda(r) = \begin{cases} 1/2 & \text{if } r \le 1/2, \\ r^2 & \text{if } r > 1/2, \end{cases} \quad \text{and} \quad f(x, y, z) = f_1(x, y) f_2(z) \quad \text{where}$$
$$f_1(x, y) = \begin{cases} 2\cos(20y) & \text{if } r \le 1/2, \\ \cos(10x) & \text{if } r > 1/2, \end{cases} \quad f_2(z) = \begin{cases} 2\cos(20z) & \text{if } z \le 0, \\ \sin(10z) & \text{if } z \ge 0. \end{cases} \tag{6.13}$$

We utilize the same discretization as in the previous 3D cylinder example truncation degree $N_p = 60$ and the quasi-optimal complexity solver for 3D cylinders introduced in Section 5. The discontinuity of the right-hand side and the Helmholtz coefficient is severe. Nevertheless, the hierarchical tensor-product FEM basis accurately approximates the right-hand side and we obtain a solution that is qualitatively accurate.

7 Conclusions

In this work we designed a sparse hp-finite element method for the disk and annulus domains. The mesh consists of an innermost disk cell and concentric annuli cells. The hierarchical FEM basis contains bubble (internal shape) functions, which are weighted multivariate orthogonal Zernike (annular) polynomials whose support is fully contained on one cell, and hat (external shape) functions which are supported on a maximum of two cells. The bubble functions encode the high-order approximation properties of the FEM whereas the hat functions enforce continuity in the solution. The basis induces sparse block-diagonal stiffness and mass matrices where the blocks correspond to the Fourier mode decoupling of the corresponding PDE operators. The discretization retains symmetry and sparsity in the induced linear systems for a number of PDEs including the Helmholtz equation with a rotationally invariant and radially discontinuous Helmholtz coefficient. Moreover, the linear systems admit an optimal complexity $\mathcal{O}(N_h N_p^2)$ factorization where N_h is the number of cells in the mesh and N_p is the truncation order on each element.

We considered a number of examples including:

1. A high-frequency Helmholtz equation with a radially discontinuous Helmholtz coefficient and right-hand side.
2. The time-dependent Schrödinger equation. The discretization is unitary preserving and, therefore, respects the conservation of energy of the system.
3. A rotationally anisotropic coefficient resulting in a non-separable Helmholtz problem.
4. A singular source term resolved with a graded mesh towards the origin.
5. The screened Poisson equation on a three-dimensional cylndrical domain with discontinuities in the right-hand side in the radial and z-directions. The basis is the tensor product of the FEM basis we developed for the disk and the continuous hierarchical basis for the interval cf. [32], [58, Ch. 2.5.2], and [52, Ch. 3.1]. Using recent results for Zernike (annular) polynomials [28, 51, 54] we obtain a setup complexity of $\mathcal{O}(N_h N_p^3 \log^2 N_p)$. Then via the ADI solver [26, 32], we derive a solve where we prove the complexity is $\mathcal{O}(N_h N_p^3 \log(N_h^{1/4} N_p))$.

In all examples we observe spectral convergence, potentially after an initial plateau, for increasing truncation degree N_p.

Acknowledgements We are grateful to Timon S. Gutleb for his contributions to the SemiclassicalOrthogonalPolynomials.jl package [42] which allowed us to build, in optimal complexity, the raising operator matrices used in this work. We are also grateful to Richard M. Slevinsky for his implementations of the quasi-optimal analysis and synthesis operators for Zernike (annular) polynomials in FastTransforms.jl [55]. IP would like to express his gratitude to Pranav Singh for the discussions on unitary preserving time-stepping schemes and for providing references that detail the stationary solutions of the Schrödinger equation. IP also thanks Daniel Fortunato for the discussions on the ADI algorithm as well as Kars Knook for sharing his Julia implementation of the ADI algorithm.

Funding Open Access funding enabled and organized by Projekt DEAL. This work was completed with the support of the EPSRC grant EP/T022132/1 "Spectral element methods for fractional differential equations, with applications in applied analysis and medical imaging" and the Leverhulme Trust Research Project Grant RPG-2019-144 "Constructive approximation theory on and inside algebraic curves and surfaces". IP was also supported by the Deutsche Forschungsgemeinschaft (DFG, German Research Foundation) under Germany's Excellence Strategy – The Berlin Mathematics Research Center MATH+ (EXC-2046/1, project ID: 390685689).

Data availability The numerical experiments were conducted in Julia and heavily rely on a number of packages [40–43, 49, 55]. For reproducibility, an implementation of the hierarchical basis as well as scripts to generate the plots and solutions can be found at SparseDiskFEM.jl [50]. The version used in this paper is archived on Zenodo [48].

Declarations

Conflict of interest The authors does not have any competing interests.

Open Access This article is licensed under a Creative Commons Attribution 4.0 International License, which permits use, sharing, adaptation, distribution and reproduction in any medium or format, as long as you give appropriate credit to the original author(s) and the source, provide a link to the Creative Commons licence, and indicate if changes were made. The images or other third party material in this article are included in the article's Creative Commons licence, unless indicated otherwise in a credit line to the material. If material is not included in the article's Creative Commons licence and your intended use is not permitted by statutory regulation or exceeds the permitted use, you will need to obtain permission directly from the copyright holder. To view a copy of this licence, visit http://creativecommons.org/licenses/by/4.0/.

References

1. Adams, R.A., Fournier, J.J.: Sobolev Spaces, second Elsevier, Amsterdam (2003)

2. Ainsworth, M., Parker, C.: Unlocking the secrets of locking: Finite element analysis in planar linear elasticity. Comput. Methods Appl. Mech. Eng. **395**, 115034 (2022). https://doi.org/10.1016/j.cma.2022.115034
3. Atkinson, K., Chien, D., Hansen, O.: Spectral Methods Using Multivariate Polynomials On The Unit Ball. CRC Press (2019). https://doi.org/10.1201/9780429344374
4. Aurentz, J.L., Slevinsky, R.M.: On symmetrizing the ultraspherical spectral method for self-adjoint problems. J. Comput. Phys. **410**, 109383 (2020). https://doi.org/10.1016/j.jcp.2020.109383
5. Babuška, I., Craig, A., Mandel, J., Pitkäranta, J.: Efficient preconditioning for the p-version finite element method in two dimensions. SIAM J. Numer. Anal. **28**(3), 624–661 (1991). https://doi.org/10.1137/0728034
6. Babuška, I., Dorr, M.R.: Error estimates for the combined h and p versions of the finite element method. Numer. Math. **37**, 257–277 (1981). https://doi.org/10.1007/BF01398256
7. Babuška, I., Szabó, B.A.: Lecture notes on finite element analysis. 1983–1985
8. Babuska, I., Szabo, B.A., Katz, I.N.: The p-version of the finite element method. SIAM J. Numer. Anal. **18**(3), 515–545 (1981). https://doi.org/10.1137/0718033
9. Bader, P., Iserles, A., Kropielnicka, K., Singh, P.: Efficient methods for linear Schrödinger equation in the semiclassical regime with time-dependent potential. Proceedings of the Royal Society A: Mathematical, Physical and Engineering Sciences **472**(2193), 20150733 (2016). https://doi.org/10.1098/rspa.2015.0733
10. Beuchler, S., Pechstein, C., Wachsmuth, D.: Boundary concentrated finite elements for optimal boundary control problems of elliptic PDEs. Comput. Optim. Appl. **51**(2), 883–908 (2012). https://doi.org/10.1007/s10589-010-9370-2
11. Beuchler, S., Pillwein, V.: Sparse shape functions for tetrahedral p-FEM using integrated Jacobi polynomials. Computing **80**(4), 345–375 (2007). https://doi.org/10.1007/s00607-007-0236-0
12. Beuchler, S., Pillwein, V., Schöberl, J., Zaglmayr, S.: Sparsity optimized high order finite element functions on simplices. Springer (2012). https://doi.org/10.1007/978-3-7091-0794-2_2
13. Beuchler, S., Schöberl, J.: New shape functions for triangular p-FEM using integrated Jacobi polynomials. Numer. Math. **103**(3), 339–366 (2006). https://doi.org/10.1007/s00211-006-0681-2
14. Boullé, N., Townsend, A.: Computing with functions in the ball. SIAM J. Sci. Comput. **42**(4), C169–C191 (2020). https://doi.org/10.1137/19M1297063
15. Boyd, J.P., Yu, F.: Comparing seven spectral methods for interpolation and for solving the Poisson equation in a disk: Zernike polynomials, Logan-Shepp ridge polynomials, Chebyshev-Fourier series, cylindrical Robert functions, Bessel-Fourier expansions, square-to-disk conformal mapping and radial basis functions. J. Comput. Phys. **230**(4), 1408–1438 (2011). https://doi.org/10.1016/j.jcp.2010.11.011
16. Brenner, S.C., Scott, L.R.: The Mathematical Theory of Finite Element Methods, volume 15 of *Texts in Applied Mathematics*. Springer New York, New York, NY, 3 edition, (2008). https://doi.org/10.1007/978-0-387-75934-0
17. Brubeck, P.D., Farrell, P.E.: A scalable and robust vertex-star relaxation for high-order FEM. SIAM J. Sci. Comput. **44**(5), A2991–A3017 (2022). https://doi.org/10.1137/21M1444187
18. Burns, K.J., Vasil, G.M., Oishi, J.S., Lecoanet, D., Brown, B.P.: Dedalus: A flexible framework for numerical simulations with spectral methods. Physical Review Research **2**(2), 023068 (2020). https://doi.org/10.1103/PhysRevResearch.2.023068
19. Cangiani, A., Dong, Z., Georgoulis, E.: hp-version discontinuous Galerkin methods on essentially arbitrarily-shaped elements. Math. Comput. **91**(333), 1–35 (2022). https://doi.org/10.1090/mcom/3667
20. Clenshaw, C.: The numerical solution of linear differential equations in Chebyshev series. In: Mathematical Proceedings of the Cambridge Philosophical Society, volume 53, pages 134–149. Cambridge University Press, (1957)
21. Dubiner, M.: Spectral methods on triangles and other domains. J. Sci. Comput. **6**, 345–390 (1991). https://doi.org/10.1007/BF01060030
22. Ellison, A.C., Julien, K.: Gyroscopic polynomials. J. Comput. Phys. 112268 (2023). https://doi.org/10.1016/j.jcp.2023.112268
23. Ellison, A.C., Julien, K., Vasil, G.M.: A gyroscopic polynomial basis in the sphere. J. Comput. Phys. **460**, 111170 (2022). https://doi.org/10.1016/j.jcp.2022.111170
24. Evans, L.C.: Partial Differential Equations, 2nd edn. American Mathematical Society, Providence (2010)
25. Fortunato, D., Hale, N., Townsend, A.: The ultraspherical spectral element method. J. Comput. Phys. **436**, 110087 (2021). https://doi.org/10.1016/j.jcp.2020.110087
26. Fortunato, D., Townsend, A.: Fast Poisson solvers for spectral methods. IMA J. Numer. Anal. **40**(3), 1994–2018 (2020). https://doi.org/10.1093/imanum/drz034
27. Gagliardo, E.: Caratterizzazioni delle tracce sulla frontiera relative ad alcune classi di funzioni in n variabili. Rendiconti del seminario matematico della universita di Padova **27**, 284–305 (1957)

28. Gutleb, T.S., Olver, S., Slevinsky, R.M.: Polynomial and rational measure modifications of orthogonal polynomials via infinite-dimensional banded matrix factorizations. Found. Comput. Maths. 1–43 (2024). https://doi.org/10.1007/s10208-024-09671-w
29. Hochbruck, M., Ostermann, A.: Exponential integrators. Acta Numer **19**, 209–286 (2010). https://doi.org/10.1017/S0962492910000048
30. Jia, L., Li, H., Zhang, Z.: Sparse spectral-Galerkin method on an arbitrary tetrahedron using generalized koornwinder polynomials. J. Sci. Comput. **91**(1), 22 (2022). https://doi.org/10.1007/s10915-022-01778-y
31. Karniadakis, G.E., Sherwin, S.: Spectral/hp element methods for computational fluid dynamics. Oxford University Press on Demand, Oxford (2005). https://doi.org/10.1093/acprof:oso/9780198528692.001.0001
32. Knook, K., Olver, S., Papadopoulos, I.P.A.: Quasi-optimal complexity hp-FEM for the Poisson equation on a rectangle, (2024). arXiv:2402.11299
33. Kwan, Y.-Y.: Efficient spectral-Galerkin methods for polar and cylindrical geometries. Appl. Numer. Math. **59**(1), 170–186 (2009). https://doi.org/10.1016/j.apnum.2008.01.003
34. Li, H., Xu, Y.: Spectral approximation on the unit ball. SIAM J. Numer. Anal. **52**(6), 2647–2675 (2014). https://doi.org/10.1137/130940591
35. Magnus, A.P.: Painlevé-type differential equations for the recurrence coefficients of semi-classical orthogonal polynomials. J. Comput. Appl. Math. **57**(1–2), 215–237 (1995). https://doi.org/10.1016/0377-0427(93)E0247-J
36. Mahajan, V.N.: Zernike annular polynomials for imaging systems with annular pupils. JOSA **71**(1), 75–85 (1981). https://doi.org/10.1364/JOSA.71.000075
37. Meyer, M.M., Medina, F.R.P.: Polar differentiation matrices for the Laplace equation in the disk under nonhomogeneous Dirichlet, Neumann and Robin boundary conditions and the biharmonic equation under nonhomogeneous Dirichlet conditions. Computers & Mathematics with Applications **89**, 1–19 (2021). https://doi.org/10.1016/j.camwa.2021.02.005
38. Molina-Meyer, M., Medina, F.R.P.: A collocation-spectral method to solve the bi-dimensional degenerate diffusive logistic equation with spatial heterogeneities in circular domains. Rendiconti dell'Istituto di Matematica dell'Università di Trieste **52**, 311–344 (2020). https://doi.org/10.13137/2464-8728/30917
39. Olver, F.W.J., Olde Daalhuis, A.B., Lozier, D.W., Schneider, B.I., Boisvert, R.F., Clark, C.W., Miller, B.R., Saunders, B.V., Cohl, H.S., McClain, M.A.: NIST Digital Library of Mathematical Functions. http://dlmf.nist.gov/, Release 1.1.4 of 2022-01-15, (2022). URL: http://dlmf.nist.gov/
40. Olver, S., et al.: ClassicalOrthogonalPolynomials.jl, (2025). URL: https://github.com/JuliaApproximation/ClassicalOrthogonalPolynomials.jl
41. Olver, S., et al.: MultivariateOrthogonalPolynomials.jl, (2025). URL: https://github.com/JuliaApproximation/MultivariateOrthogonalPolynomials.jl
42. Olver, S., Gutleb, T.S., Papadopoulos, I.P.A.: SemiclassicalOrthogonalPolynomials.jl, (2025). URL: https://github.com/JuliaApproximation/SemiclassicalOrthogonalPolynomials.jl
43. Olver, S., Papadopoulos, I.P.A.: PiecewiseOrthogonalPolynomials.jl, (2025). URL: https://github.com/JuliaApproximation/PiecewiseOrthogonalPolynomials.jl
44. Olver, S., Slevinsky, R.M., Townsend, A.: Fast algorithms using orthogonal polynomials. Acta Numer **29**, 573–699 (2020). https://doi.org/10.1017/S0962492920000045
45. Olver, S., Townsend, A.: A fast and well-conditioned spectral method. SIAM Rev. **55**(3), 462–489 (2013). https://doi.org/10.1137/120865458
46. Olver, S., Townsend, A., Vasil, G.: A sparse spectral method on triangles. SIAM J. Sci. Comput. **41**(6), A3728–A3756 (2019). https://doi.org/10.1137/19M1245888
47. Ortiz, E.L.: The tau method. SIAM J. Numer. Anal. **6**(3), 480–492 (1969). https://doi.org/10.1137/0706044
48. Papadopoulos, I.P.A.: ioannisPApapadopoulos/SparseDiskFEM.jl: v0.0.2, May 2025. https://doi.org/10.5281/zenodo.15348520
49. Papadopoulos, I.P.A.: RadialPiecewisePolynomials.jl, 2025. URL: https://github.com/ioannisPApapadopoulos/RadialPiecewisePolynomials.jl
50. Papadopoulos, I.P.A.: SparseDiskFEM.jl, 2025. URL: https://github.com/ioannisPApapadopoulos/SparseDiskFEM.jl
51. Papadopoulos, I.P.A., Gutleb, T.S., Slevinsky, R.M., Olver, S.: Building hierarchies of semiclassical Jacobi polynomials for spectral methods in annuli. SIAM J. Sci. Comput. **46**(6), A3448–A3476 (2024). https://doi.org/10.1137/23M160846X
52. Schwab, C.: p-and hp-finite element methods: Theory and applications in solid and fluid mechanics. Clarendon Press, United Kingdom (1998)

53. Shen, J.: Efficient spectral-Galerkin methods III: Polar and cylindrical geometries. SIAM J. Sci. Comput. **18**(6), 1583–1604 (1997). https://doi.org/10.1137/S1064827595295301
54. Slevinsky, R.M.: Fast and backward stable transforms between spherical harmonic expansions and bivariate Fourier series. Appl. Comput. Harmon. Anal. **47**(3), 585–606 (2019). https://doi.org/10.1016/j.acha.2017.11.001
55. Slevinsky, R.M., et al.: FastTransforms.jl, 2025. URL: https://github.com/JuliaApproximation/FastTransforms.jl
56. Snowball, B., Olver, S.: Sparse spectral and-finite element methods for partial differential equations on disk slices and trapeziums. Stud. Appl. Math. **145**(1), 3–35 (2020). https://doi.org/10.1111/sapm.12303
57. Snowball, B., Olver, S.: Sparse spectral methods for partial differential equations on spherical caps. Transactions of Mathematics and its Applications **5**(1), tnab001 (2021). https://doi.org/10.1093/imatrm/tnab001
58. Szabó, B., Babuška, I.: Introduction to finite element analysis: formulation, verification and validation, vol. 35. John Wiley & Sons, New York (2011)
59. Tatian, B.: Aberration balancing in rotationally symmetric lenses. JOSA **64**(8), 1083–1091 (1974). https://doi.org/10.1364/JOSA.64.001083
60. Vasil, G.M., Burns, K.J., Lecoanet, D., Olver, S., Brown, B.P., Oishi, J.S.: Tensor calculus in polar coordinates using Jacobi polynomials. J. Comput. Phys. **325**, 53–73 (2016). https://doi.org/10.1016/j.jcp.2016.08.013
61. Wilber, H., Townsend, A., Wright, G.B.: Computing with functions in spherical and polar geometries. II The disk. SIAM J. Sci. Comput. **39**(3), C238–C262 (2017). https://doi.org/10.1137/16M1070207
62. Wiss, J.E.: Quantum mechanics in multidimensions, 2015. URL: https://courses.physics.illinois.edu/phys485/fa2015/web/dimensions.pdf

Publisher's Note Springer Nature remains neutral with regard to jurisdictional claims in published maps and institutional affiliations.